Electronic Supplementary Information (ESI) for
Coulomb interactions for mediator-enhanced sensitized triplet-triplet annihilation upconversion in solution

Felix Glaser, Matthias Schmitz and Christoph Kerzig*

Table of contents

1.   General experimental details

All reagents and substrates given below (section 3.1) were purchased from BLDPharm, FischerScientific or Sigma-Aldrich/Merck in "reagent grade" purity or better and were used as received. $[Ru(phen)_3](PF_6)_2$ was synthesized from $[Ru(phen)_3]Cl_2$ (Sigma-Aldrich, 98%) following a literature procedure.[1] 1-Pyrenesulfonic acid sodium salt (>97%) was purchased from Sigma-Aldrich; 9,10-diphenylanthracene (DPA, 99%) was purchased from Alfa Aesar and ammonium hexafluorophosphate (NH_4PF_6, 98%) was purchased from abcr GmbH. Spectroscopic measurements were performed with solvents of HPLC or analytical reagent grade purity. Deuterated solvents from Deutero and Sigma-Aldrich were used for NMR measurements. Dimethylformamide (DMF) was obtained from Fischer Scientific in analytical reagent grade purity (>99.5%). NMR spectra were recorded on a Bruker Avance DRX 300 or a Bruker Avance II 400 MHz spectrometer. ^{1}H NMR spectra were calibrated using the residual non-deuterated solvent and the chemical shifts are given as δ values in ppm. All coupling constants J are given in Hertz (Hz).

Steady-state emission measurements were performed using a Perkin Elmer FL-6500 spectrometer at room temperature (295 ± 2 K). Neutral density filters (Thorlabs) were installed in front of the detector to adjust the respective emission intensity to the linear detection regime if required. Absorption spectra were recorded with a Perkin Elmer LAMBDA 365 UV-Vis spectrophotometer. All spectra were recorded at room temperature (295 ± 2 K). All solutions for optical spectroscopy were purged with argon (Nippon Gases 5.0) for at least 10 minutes before the measurements and sealed under inert gas in 1.0 cm pathlength septum cap quartz glass cuvettes. For quantitative measurements, the emission spectra were corrected for the wavelength-dependent sensitivity of the emission spectrometer.[2]

The emission lifetimes for the catalyst and other compounds were recorded with a mini-τ spectrometer from Edinburgh Instruments (time-correlated single photon counting TCSPC technique), with pulsed lasers (EPL-375, pulse-width 58.3 ps, average power 5 mW, λ_{ex} = 371 nm; EPL-450, pulse-width 74.5 ps, average power 5 mW, λ_{ex} = 446 nm) for excitation and the integrated bandpass filters for detection centered at 450 nm, 500 nm, 550 nm, 600 nm, and 650 nm with ~50 nm band width.

For the laser flash photolysis (LFP) measurements an LP980-KS apparatus form Edinburgh Instruments was used to measure transient absorption and time-resolved emission spectra. The energy of the 532 nm laser pulse (frequency-doubled Nd:YAG laser from Quantel) was modified by the Q-switch delay. Excitation at 355 nm was performed with a frequency-triplet Nd:YAG laser (Litron Nano LG 300-10). Beam expanders (Thorlabs) were used to ensure homogenous excitation in the detection volume and excitation occurred with typical pulse energies of ~20 mJ. The laser pulse duration was ~5 ns and the pulse frequency was 10 Hz. Detection of transient spectra was performed with an iCCD camera from Andor and kinetic traces were recorded at a single wavelength with a photomultiplier tube. Unless otherwise stated, time-resolved spectra were time-integrated for 200 ns. The spectroscopic experiments were performed at 293 K using a cuvette holder that allows temperature control. For steady-state Stern–Volmer analysis the respective lifetime in the absence of quencher was determined with the same sample to ensure identical conditions for both measurements.

As light source for continuous wave (cw) laser experiments and photocatalysis, a 520 nm cw laser (Roithner Lasertechnik) with precisely adjustable radiative power was used (optical output up to 800 mW). For

measurements with a 525 nm LED, the light source from Kessil (PR160L LED, 525 nm, 40 W) was equipped with a 495 nm longpass filter (Thorlabs) between the lamp and the sample. Emission spectra of the green LED and the 520 nm cw laser were measured by irradiating a water-containing cuvette in the FL-6500 instrument and recording the Rayleigh scattering light. For the measurements of the triplet-triplet annihilation upconversion power dependencies, the FL-6500 spectrometer was equipped with the abovementioned cw laser (Roithner Lasertechnik) or the Kessil LED as light source. Modifications of the light intensity were performed by the introduction of one or more neutral density filters (Newport and Thorlabs, ND0.1 – ND2.0) in the beam path between the light source and the sample. The detected emission was adjusted by neutral density filters (Thorlabs) to the linear regime of the detector. The setup is shown in Figure S1.The beam size for the cw laser was reported by in the technical specifications of the laser (0.03 cm^2),[3] while the power density of the LED was estimated from the averaged general intensity map (~100 mW cm^2 at ~7 cm distance) provided by the manufacturer.

2.   Measurement and irradiation setup

The setup for power-dependent measurements and upconversion quantum yields with the green cw laser (514 nm) and the green LED (525 nm) setup are given in Figure S1. Modifications of the light intensity were performed by the introduction of one or more neutral density filters (Newport and Thorlabs, ND0.1 – ND2.0) in the beam path between the light source and the sample.
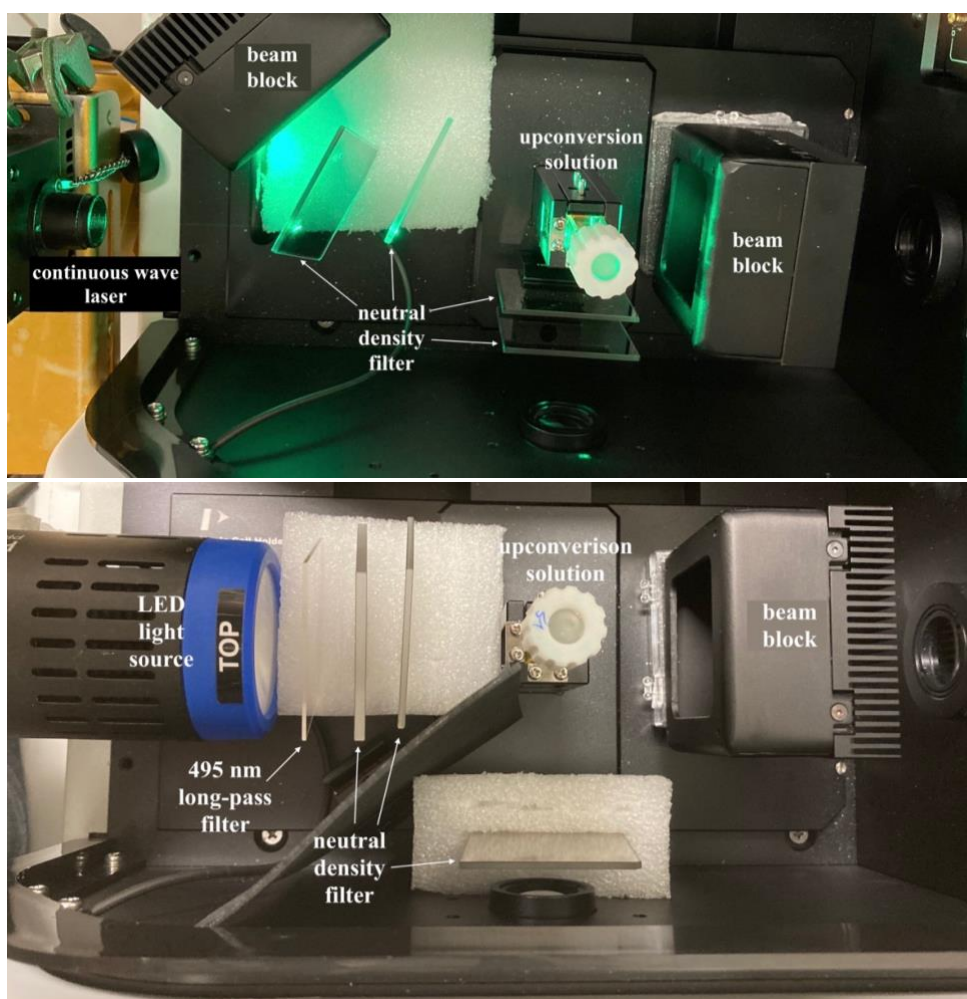
Figure S1. Irradiation setup for power-dependent steady-state emission measurements with a cw laser (top) and a LED light source (bottom).
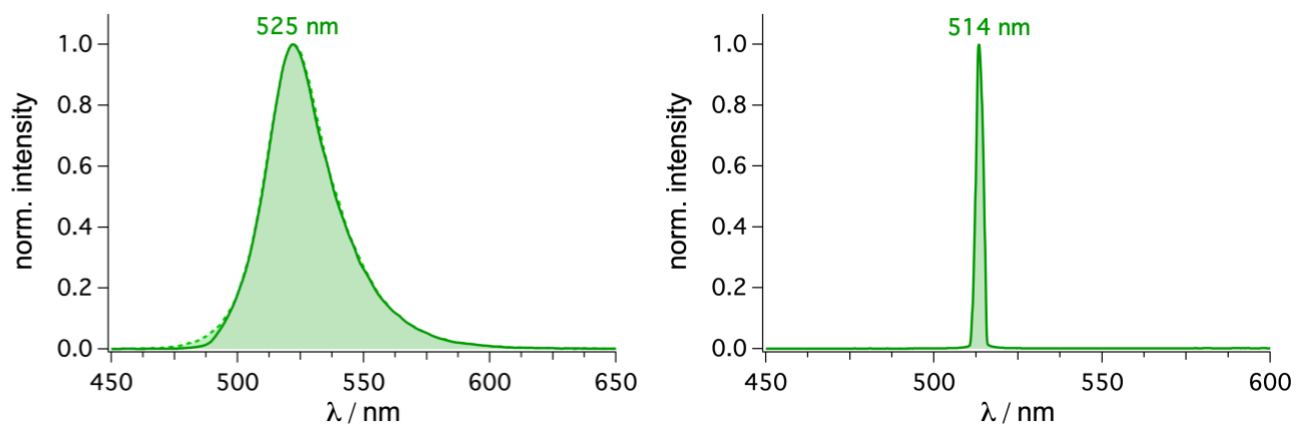
Figure S2. Left: Emission spectrum of the 525 nm Kessil LED without (dotted line) and with a 495 nm longpass filter (Newport) installed between the light source and the detector. Right: Emission spectrum of the green cw laser.
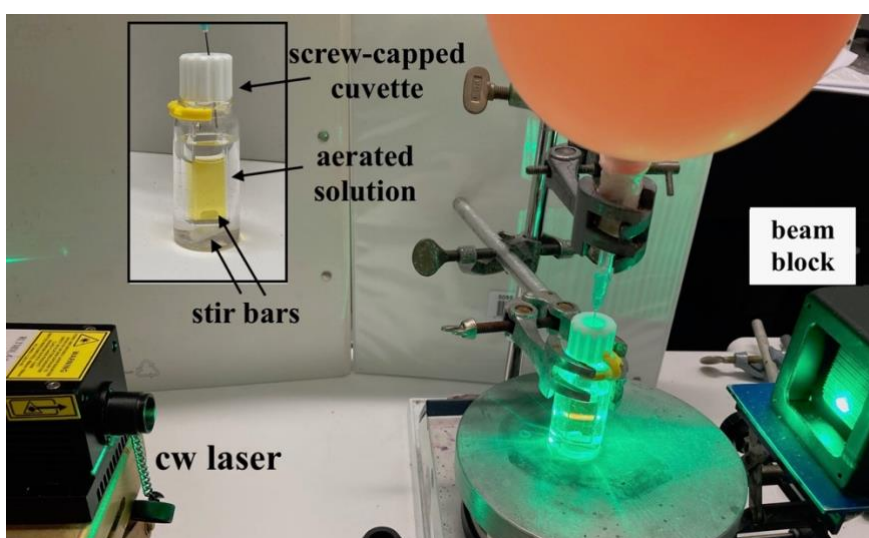
Figure S3. Irradiation setup for continuous laser (cw) irradiation for aerated photo(redox) catalysis in a two-chamber system.

3. Synthetic procedures and photocatalysis experiments

3.1. Synthetic procedures

3.1.1. Synthesis of [Ru(phen)₃](PMS)₂
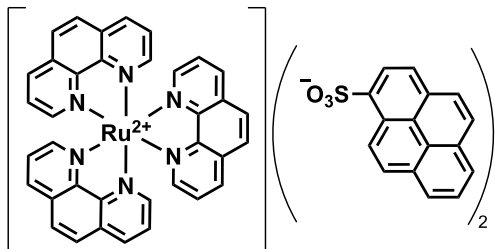
Following a modified synthetic procedure,[1] [Ru(phen)$_3$]Cl$_2$•xH$_2$O (50.0 mg, 68.4 μmol, 1.0 eq) and sodium pyrene-1-sulfonate (NaPMS, 41.7 mg, 136.9 μmol, 2.0 eq) were each dissolved in a minimal amount of ultrapure Millipor MilliQ water and subsequently combined in an Erlenmeyer flask. An instantaneous formation of an orange-red precipitate is observed, and after stirring for 30 minutes at room temperature the precipitate was filtered off and washed with small portions of water (3x). The isolated product was dried *in-vacuo* to yield a dark red crystalline solid [Ru(phen)$_3$](PMS)$_2$ (52.1 mg, 68.4 μmol, 63 %).

¹H NMR (300 MHz, DMSO-d$_6$) δ 9.17 (d, $J_{H,H}$ = 9.4 Hz, 2H), 8.76 (d, $J_{H,H}$ = 7.2 Hz, 6H), 8.50 (d, $J_{H,H}$ = 8.0 Hz, 2H), 8.37 (s, 6H), 8.30 (dd, $J_{H,H}$ = 7.7 Hz, $J_{H,H}$ = 1.6 Hz, 4H), 8.25 – 8.13 (m, 8H), 8.13 – 8.02 (m, 8H), 7.75 (dd, $J_{H,H}$ = 8.2 Hz, $J_{H,H}$ = 5.3 Hz, 6H).

¹³C NMR (75 MHz, DMSO-d$_6$): δ 152.7, 147.2, 142.0, 136.8, 131.2, 130.4, 130.1, 128.0, 127.6, 127.3, 126.9, 126.7, 126.3, 126.2, 125.3, 125.3, 124.8, 124.2, 123.7 ppm.

The photophysical characterization is provided in the main manuscript and summarized in Table S1.
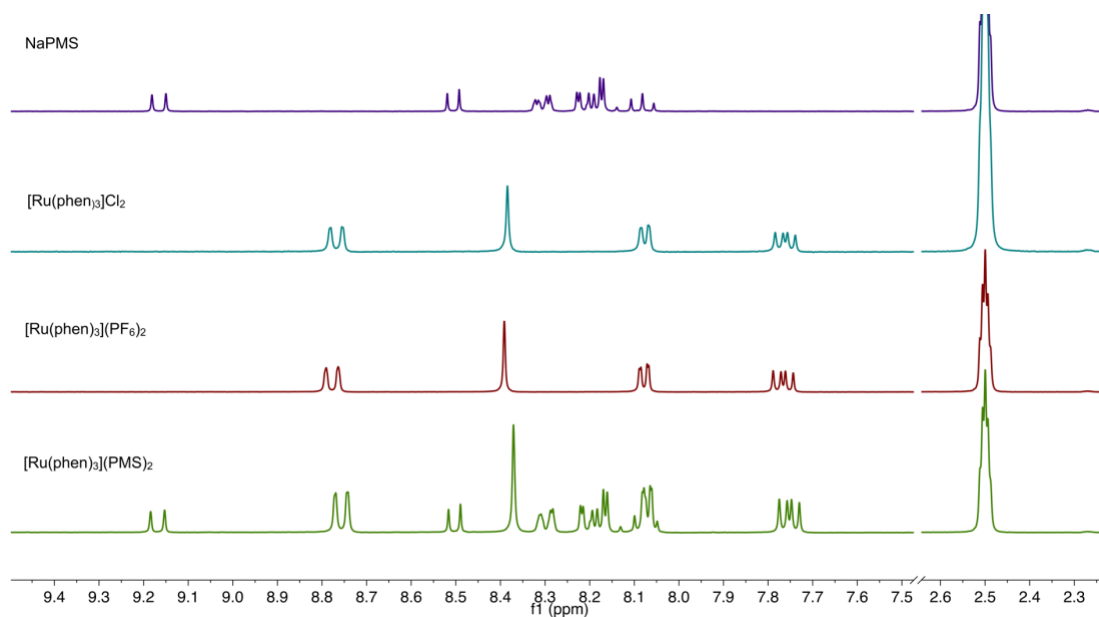
Figure S4. ¹H NMR spectra of NaPMS, [Ru(phen)$_3$]Cl$_2$, [Ru(phen)$_3$](PF$_6$)$_2$ and [Ru(phen)$_3$](PMS)$_2$ in DMSO-d$_6$.

3.1.2. Light-driven photocatalytic triphenylphosphine oxygenation *via* sTTA-UC

Photoredox catalysis stock solution: An oven-dried screw-capped amber glass bottle was charged with triphenylphosphine (264 mg, 1.01 mmol, 1.0 eq.) naphthalene (257 mg, 2.01 mmol, 2.0 eq.) and 9,10-dicyanoanthracene (DCA, 5.70 mg, 25.0 µmol, 0.025 eq.), 100 mL of acetonitrile were added and all components were dissolved by sonication. The stock solution was stored in the dark under argon up to several hours, while for new measurement days a fresh stock solution was prepared.

Upconversion solutions: The different upconversion solutions prepared from stock solutions in dimethylformamide. The stock solution of $[Ru(phen)_3](PF_6)_2$ (150 µM), NaPMS (7.5 mM) and 9,10-diphenylanthracene (DPA, 300 µM) were stored in the dark.

For each measurement the respective amount of $[Ru(phen)_3](PF_6)_2$, NaPMS and DPA from the stock solutions was combined in a screw-capped cuvette (typically 0.7 mL each) and the resulting solution was diluted to a total volume of 2.1 mL of DMF. The cuvette was equipped with a tiny stirring bar, sealed with a rubber septum and the solutions were purged with argon for at least 10 minutes. A balloon of argon was installed for the duration of the reaction on the cuvette. Then a glass vial was equipped with a stir bar and 10 mL of the photoredox catalysis stock solution and the cuvette was placed inside and fixed in front of the laser (Figure S3). The stirred solutions were irradiated for 20 minutes. After irradiation the reaction solutions were transferred to a round bottom flask and the solvent was removed under reduced pressure. The crude reaction mixture was analyzed by ^{1}H NMR spectroscopy. Sample NMR spectra are shown in section 5.

3.1.3. Light-driven photocatalytic anthracene endoperoxide formation *via* sTTA-UC

Photocatalysis solutions: For the anthracene stock solution, 9,10-dimethylanthracene (DMAn, 7.22 mg, 350 µmol) was dissolved in 35 mL of acetonitrile (1.0 mM). For the photocatalyst stock solution, 2,7-dimethoxy-9H-thioxanthen-9-one (MeOTX, 3.40 mg, 12.5 µmol) was dissolved in 5 mL of acetonitrile (2.5 mM). The stock solutions were stored in the dark.

Upconversion solutions: The different upconversion solutions were mixed from stock solutions in dimethylformamide. The stock solution of $[Ru(phen)_3](PF_6)_2$ (150 µM), NaPMS (7.5 mM) and DPA (300 µM) were stored in the dark.

For each measurement the respective amount of $[Ru(phen)_3](PF_6)_2$, NaPMS and DPA from the stock solutions was combined in a screw-capped cuvette (typically 0.7 mL each) and resulting solution was diluted to a total volume of 2.1 mL of DMF. The cuvette was equipped with a tiny stirring bar, sealed with a rubber septum and the solutions were purged with argon for at least 10 minutes. A balloon of argon was installed for the duration of the reaction on the cuvette. Then a glass vial was equipped with a stir bar and the 9,10-dimethylanthracene stock solution (10 mL) and photocatalyst stock solution (200 µL). The cuvette was placed inside of the glass vial and fixed in front of the laser (Figure S3). Before the measurements and after specific irradiation times the irradiation was interrupted and UV-vis absorption spectra of the photocatalysis solution were recorded in 2 mm cuvettes. After the measurements the solutions were transferred back to the glass vial and the irradiation was continued.

Note for both reactions: In the case of a high concentrations of DPA (5 mM), the respective amount of DPA was directly added to the cuvette and the solution was stirred while degassing.

4. Optical spectroscopic measurements

4.1. Spectroscopic properties of sensitizer, mediator and annihilator

4.1.1. Photophysical characterization of the main system

All measurements were performed in de-aerated solvents at room temperature.
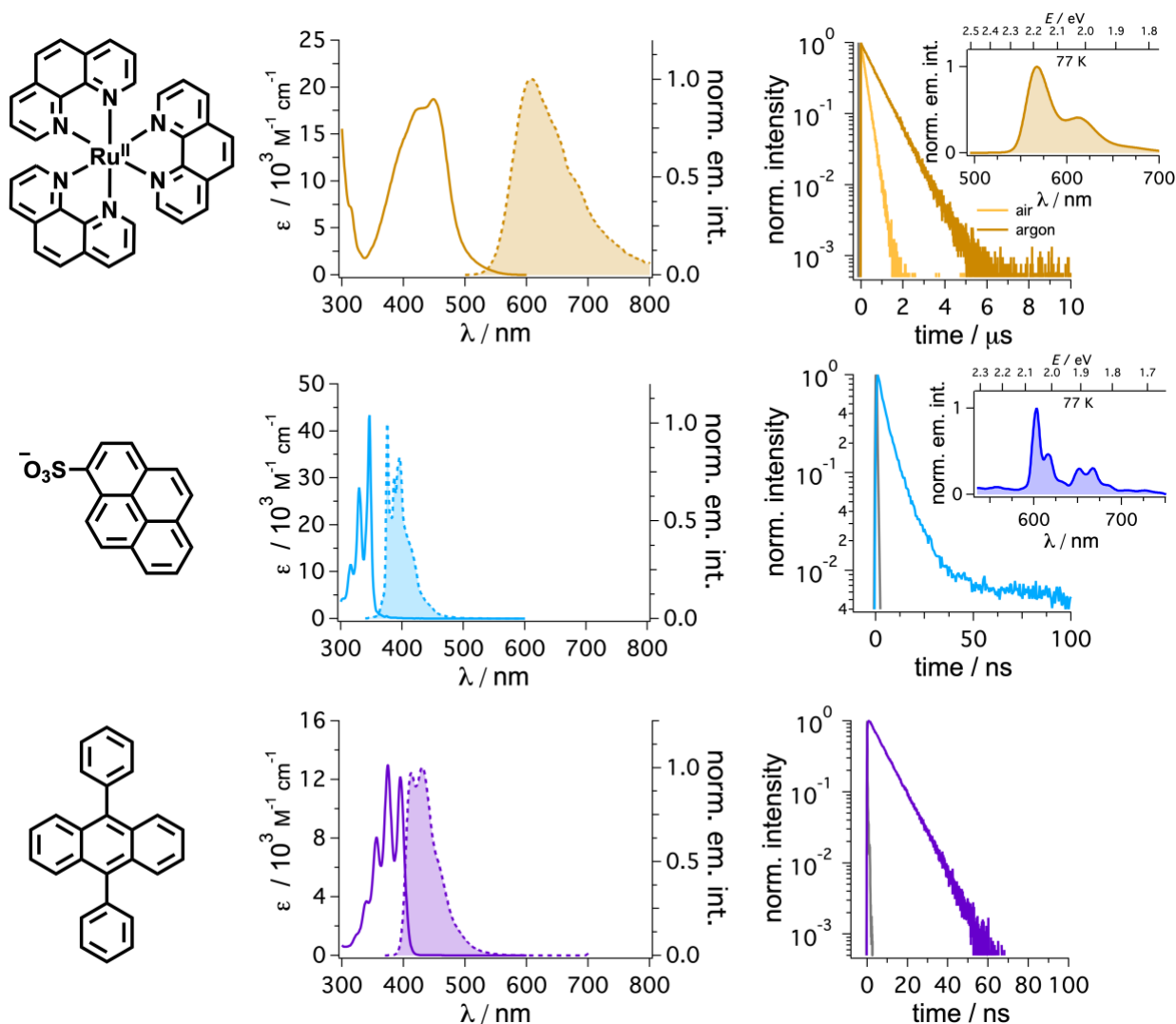
Figure S5. UV-vis absorption and emission spectra as well as emission lifetimes of [Ru(phen)₃](PF₆)₂ (top), NaPMS (middle) and DPA (bottom) in de-aerated DMF. The emission decay curves are measured by single photon counting with a suitable filter and the respective IRF traces are provided in gray. Low temperature emission spectra in frozen matrix ([Ru(phen)₃]²⁺ and PMS in 4:1 ethanol-methanol) are presented as insets (λ$_{ex}$ = 355 nm). The main results are also summarized in Table S1.

Table S1. Overview of photophysical properties at 20 °C in dimethylformamide.

compound	λ_{abs} (ε) / nm (10^3 M^{-1} cm^{-1})	λ_{em} / nm	Φ_{Ar} / % [a]	Φ_{air} / % [a]	τ_0 / ns	$E_{0,0}$ / eV [b]
[Ru(phen)$_3$](PF$_6$)$_2$	450 (18.7)	606	6.77 ±0.05	1.75 ±0.12	728 [d]	2.19 (E_T)
NaPMS	330 (28.0)	374	57.3 ±0.8	- [c]	6.67 (99.3 %)	3.42 (E_S)
	347 (43.3)	395			570 (0.7 %)	2.06 (E_T)
DPA	356 (8.08)	412	88.2 ±0.3	- [c]	8.60	3.08 (E_S)
	374 (13.0)	431				1.77 (E_T)[4]
	395 (12.2)					
[Ru(phen)$_3$](PMS)$_2$ [e]	330 (55.0)	607	- [f]	- [f]	- [f]	- [c]
	347 (81.4)					
	449 (16.3)					

a) Photoluminescence quantum yields of [Ru(phen)$_3$](PF$_6$)$_2$ were determined relative to an aerated solution of [Ru(bpy)$_3$](PF$_6$)$_2$ in acetonitrile (Φ = 0.018)[5]. Photoluminescence quantum yields of DPA were determined relative to a de-aerated solution of perylene in ethanol (Φ = 0.92).[4,6] b) The energies of first singlet excited states $E_{0,0}$ for NaPMS and DPA were estimated from the intersections of normalized UV-vis and emission spectra. The triplet excited state for [Ru(phen)$_3$]$^{2+}$ and PMS was estimated from the emission maximum at 77 K. c) These values were not determined. d) Emission lifetime in de-aerated solution. In aerated solution the emission lifetime of [Ru(phen)$_3$]$^{2+}$ is 220 ns. e) Corresponding datasets are presented in Figure 3 of the main manuscript. f) Lifetime and quantum yield are highly concentration-dependent and therefore not provided here.

The results obtained for [Ru(phen)$_3$](PF$_6$)$_2$,[7–10] PMS,[11] and DPA[12,13] are in line with the literature reports, taking minor solvent effects into account.

4.1.2. Photophysical characterization of other investigated catalysts and compounds

Table S2. Overview of photophysical properties at 20 °C in acetonitrile.

compound	λ_{abs} (ε) / nm (10^3 M^{-1} cm^{-1})	λ_{em} / nm	τ_0 / ns	$E_{0,0}$ / eV [a]
DCA	373 (10.6)	434	13.1	2.91 (E_S)
	395 (10.3)	459		
	419 (11.3)			
DMAn	358 (5.03)	406	16.8	3.09 (E_S)
	376 (8.30)	426		
	398 (7.83)			
MeOTX	414 (5.0)	457	7940 (57.5%) [b]	2.87 (E_S)
			33800 (42.5%) [b]	2.38 (E_T)[14]

a) The energies of first singlet excited states $E_{0,0}$ for DCA, DMAn and MeOTX were estimated from the intersections of normalized UV-vis and emission spectra. b) Lifetime estimated based on the transient absorption decay, for details see Figure S6.

The spectroscopic datasets of DCA,[15,16] DMAn,[17] and MeOTX[14] are in line with the literature, taking minor solvent effects into account.
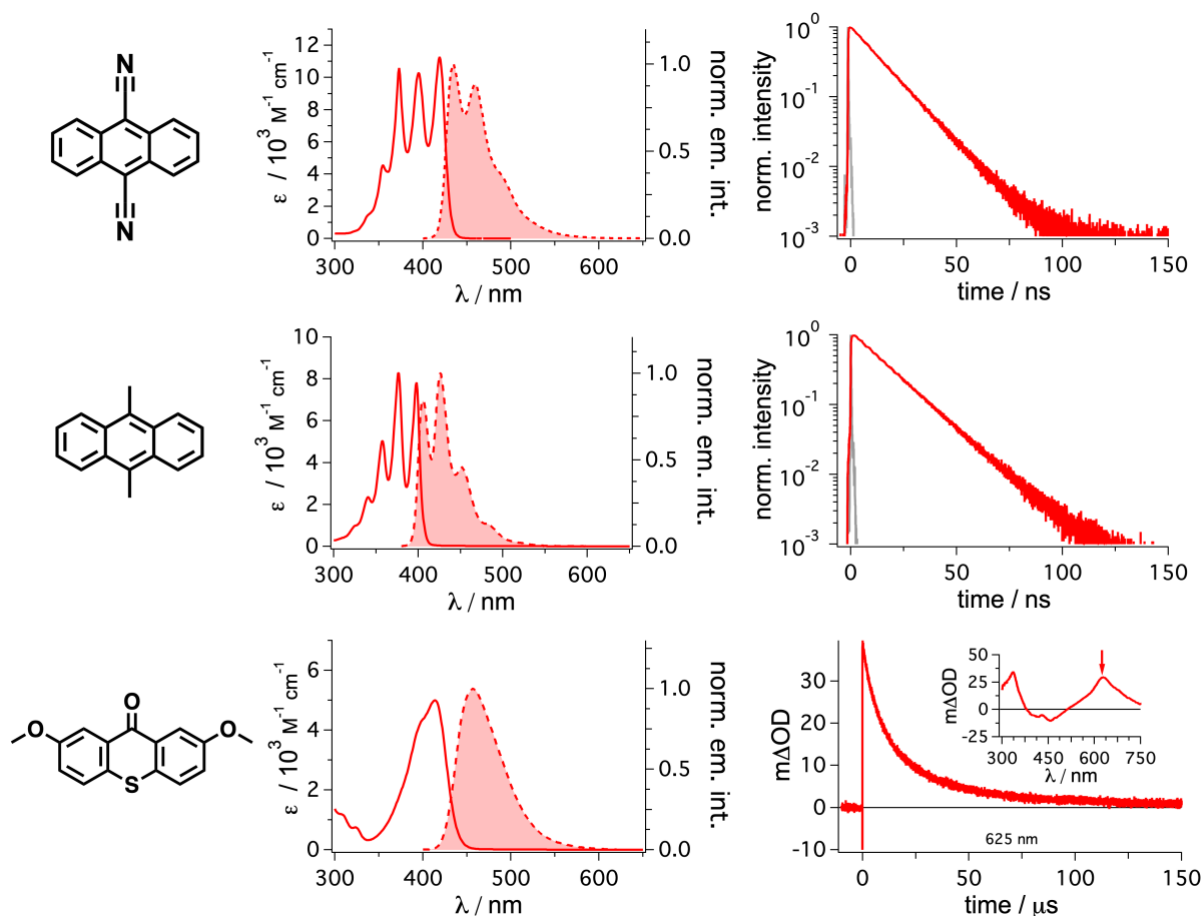
Figure S6. UV-vis absorption and emission spectra and emission lifetimes of DCA (top), DMAn (bottom) and MeOTX (bottom) in de-aerated acetonitrile. The emission decay curves of DCA and DMAn are measured by single photon counting with a suitable filter; the respective instrument response function (IRF) is provided in gray color. The triplet lifetime of MeOTX is measured by transient absorption spectroscopy (200 μM MeOTX, excitation at 355 nm, detection at 635 nm, the transient absorption spectrum measured 10 ns after laser pulse is displayed as inset. The main results are also summarized in Table S2.

4.2. Mechanistic investigations of mediated energy transfer

4.2.1. General overview
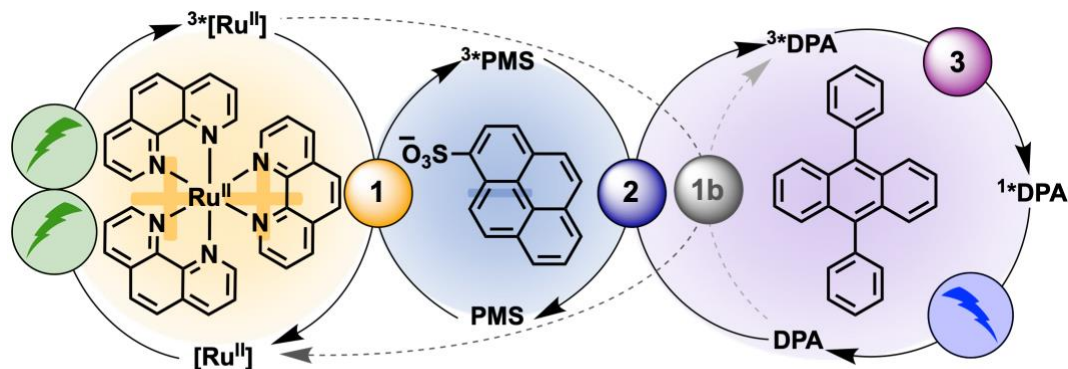
Figure S7. The key elementary reaction steps including (1) triplet-triplet energy transfer (TTET) from the sensitizer to the mediator, (2) TTET from the mediator to the annihilator and (3) triplet-triplet annihilation (TTA) are distinguished with different colored cycles. The alternative direct triplet-triplet energy transfer from $^{3*}[Ru(phen)_3]^{2+}$ to DPA is included in gray as step 1b. The determined rate constants for the different elementary steps are provided in Table S3. The same figure is provided as Figure 2a in the main manuscript.

4.2.2. Overview: triplet-triplet energy transfer from $^{3*}[Ru(phen)_3]^{2+}$

Table S3. Summary of relevant data and energy transfer rate constants. [a]

| step no.	general description	symbol	k / M^{-1} s^{-1} [b]	k / M^{-1} s^{-1} [c]	Figure
1	TTET from $^{3*}[Ru(phen)_3]^{2+}$ to PMS	k_{TTET}	$9.1 \cdot 10^9$	$6.1 \cdot 10^9$	Figure S9 Figure S8
1	Back-TTET from ^{3*}PMS to $[Ru(phen)_3]^{2+}$	k_{bTTET}	$\sim 4 \cdot 10^8$	-	Figure S15
1b	TTET from $^{3*}[Ru(phen)_3]^{2+}$ to DPA	k_{TTET}	$2.0 \cdot 10^9$	$2.1 \cdot 10^9$	Figure S11 Figure S10
2	TTET from ^{3*}PMS to DPA	k_{TTET}	$2.0 \cdot 10^9$	-	Figure S37
3	TTA-UC of ^{3*}DPA	k_{TTA}	$2.4 \cdot 10^9$	-	Figure S40
2b	TTA-UC of ^{3*}PMS	k_{TTA}	$3.1 \cdot 10^9$	-	Figure S39
1 Ref Py	TTET from $^{3*}[Ru(phen)_3]^{2+}$ to Py	k_{TTET}	$1.4 \cdot 10^9$	$9.2 \cdot 10^8$	Figure S20 Figure S19
1 with DPA	TTET from $^{3*}[Ru(phen)_3]^{2+}$ to PMS in the presence of 100 µM DPA	k_{TTET}	$9.2 \cdot 10^9$	$7.8 \cdot 10^9$	Figure S17 Figure S18

a) The unquenched excited state lifetimes (τ_0) of $[Ru(phen)_3]^{2+}$ is presented in Table S1 and the triplet state lifetimes of PMS and DPA are in Figure S39 and Figure S40. b) Time-resolved measurements. c) Steady-state measurements.

4.2.3. Triplet-triplet energy transfer from $^{3*}[Ru(phen)_3]^{2+}$ to PMS

Further information concerning <u>step 1</u> (TTET) in Figure S7 is given here.
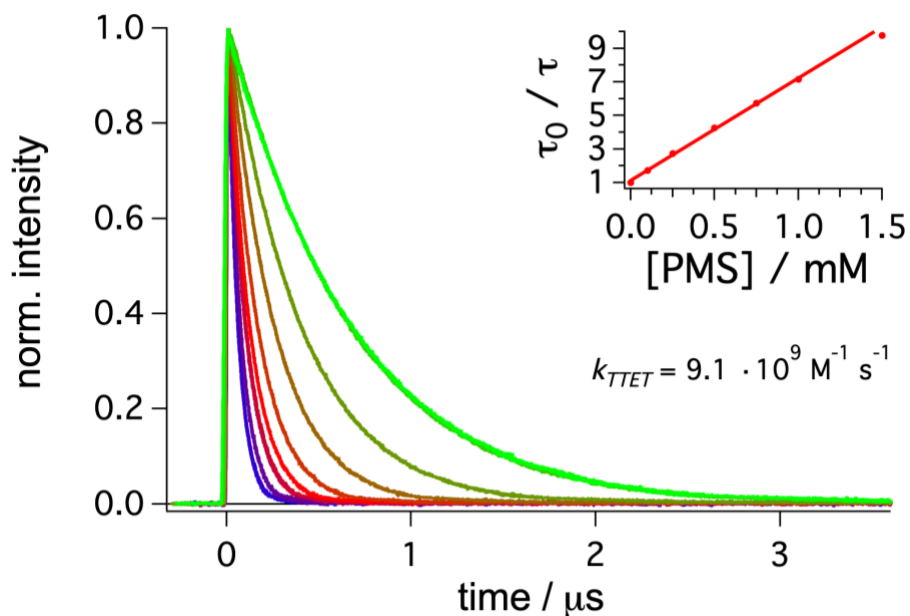
Figure S8. Emission lifetime quenching of $^{3*}[Ru(phen)_3]^{2+}$ by **PMS**. $[Ru(phen)_3]^{2+}$ (50 μM) in de-aerated dimethylformamide was excited at 532 nm and the emission decay was monitored at 600 nm in the absence (green) and in the presence of different concentrations of PMS (0.05, 0.10, 0.25, 0.5, 0.75, 1.0, 1.5 mM). The Stern−Volmer plot obtained from this data set and and the resulting quenching rate constant are given in the inset.

Figure S9. Steady-state emission quenching of $^{3*}[Ru(phen)_3]^{2+}$ by **PMS**. $[Ru(phen)_3]^{2+}$ (50 μM) in de-aerated dimethylformamide was excited at 490 nm and the emission was monitored in the absence (green) and in the presence of different concentrations of PMS (0.1, 0.25, 0.5, 0.75, 1.0, 1.5 mM). The Stern−Volmer plot obtained from this data set and and the resulting quenching rate constant (with τ_0 taken from Figure S8) are given in the inset.

4.2.4. Triplet-triplet energy transfer from $^{3*}[Ru(phen)_3]^{2+}$ to DPA
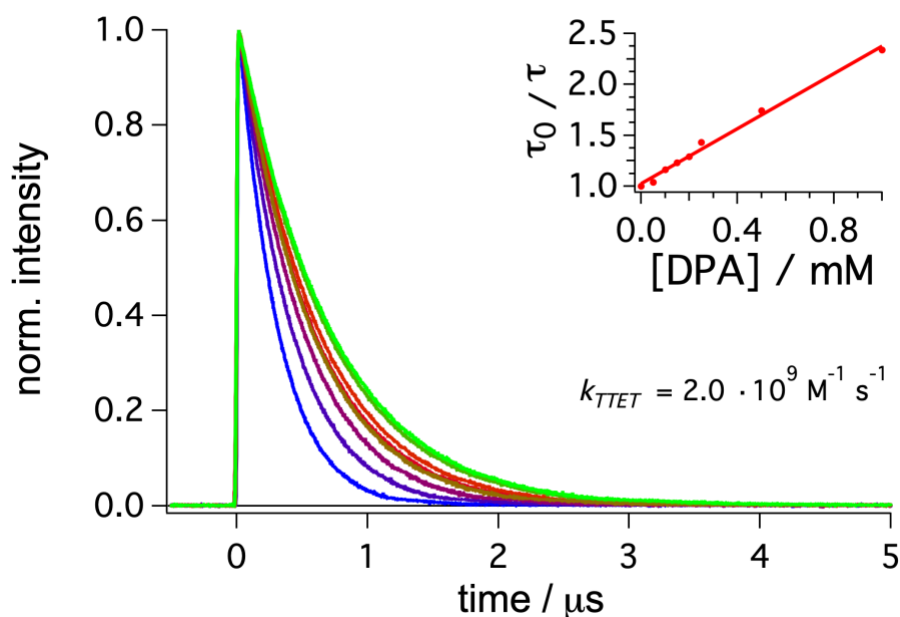
Figure S10. Emission lifetime quenching of $^{3*}[Ru(phen)_3]^{2+}$ by **DPA**. $[Ru(phen)_3]^{2+}$ (50 μM) in de-aerated dimethylformamide was excited at 532 nm and the emission decay was monitored at 600 nm in the absence (green) and in the presence of different concentrations of DPA (0.05, 0.10, 0.15, 0.20, 0.25, 0.5, 1.0 mM). The Stern–Volmer plot obtained from this data set and and the resulting quenching rate constant are given in the inset.
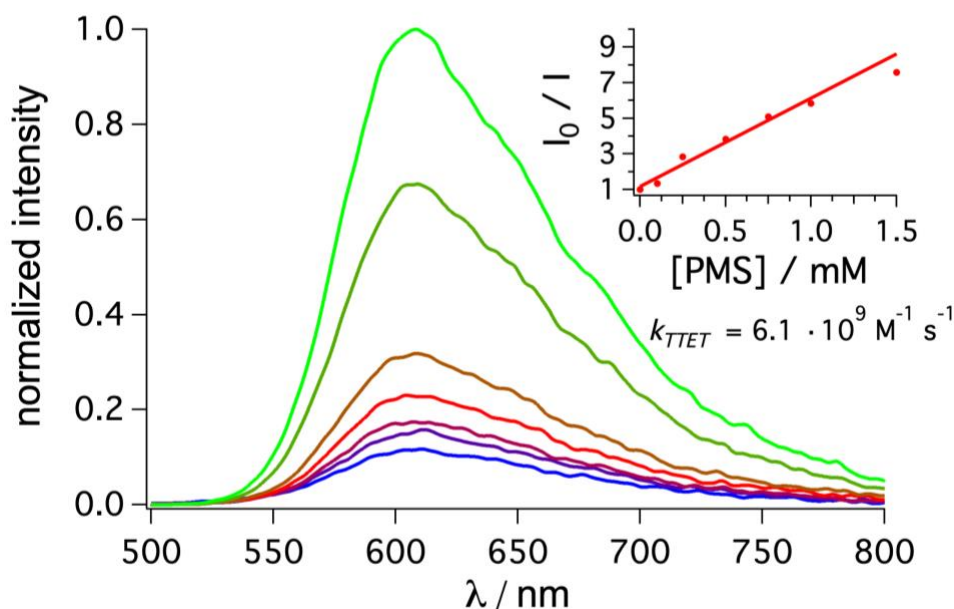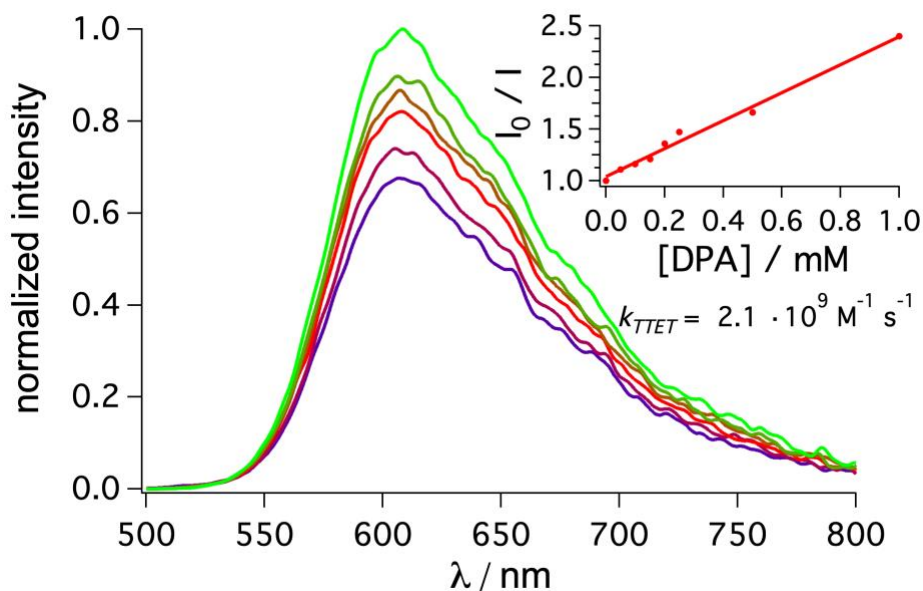

Figure S11. Steady-state emission quenching of $^{3*}[Ru(phen)_3]^{2+}$ by **DPA**. $[Ru(phen)_3]^{2+}$ (50 μM) in de-aerated dimethylformamide was excited at 490 nm and the emission was monitored in the absence (green) and in the presence of different concentrations of DPA (0.05, 0.10, 0.15, 0.20, 0.25, 0.5, 1.0 mM). The Stern–Volmer plot obtained from this data set and and the resulting quenching rate constant (with τ_0 taken from Figure S10) are given in the inset.
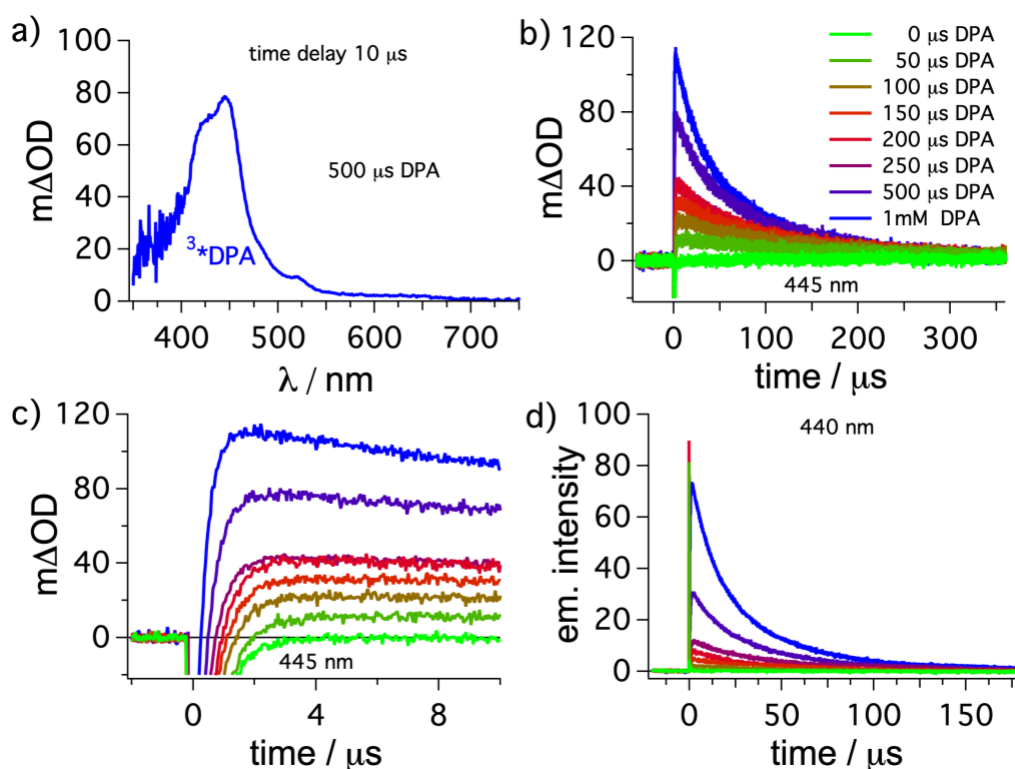
Figure S12. Triplet state formation and decay of ^{3*}DPA. [Ru(phen)$_3$]$^{2+}$ (50 μM) in de-aerated dimethylformamide was excited at 532 nm and the transient absorption spectrum (a) was recorded in the presence of DPA (500 μM), time-integrated over 200 ns. (b+c) The kinetic transient absoprtion signals with different concentrations of DPA were monitored over 350 μs (b) and 10 μs (c) at the maximum of ^{3*}DPA (445 nm).[4] d) The kinetics of delayed emission detected at 440 nm were measured for the same concentrations of DPA as indicated in (b).

As expected also from Figure 3 of the main manuscript, the characteristic transient absorption spectrum of ^{3*}DPA with a maximum at 445 nm is detected with a 10 μs time delay after the laser pulse for [Ru(phen)$_3$]$^{2+}$ (50 μM) in de-aerated dimethylformamide excited at 532 nm in the prescene of 500 μM DPA (Figure S12a). With an increasing concentration of DPA as quencher, the transient absorption intensity increases at the absorption maximum of ^{3*}DPA (445 nm, Figure S12b) and the formation is also faster (Figure S12c). Increasing delayed emission intensities (Figure S13c) are therefore also detectable with increasing concentration of DPA.

4.2.5. Back energy transfer from ^{3*}PMS to [Ru(phen)]$^{2+}$

From the time-resolved emission spectra of [Ru(phen)$_3$]$^{2+}$ (50 μM) in de-aerated dimethylformamide excited at 532 nm in the prescene of various concentrations of PMS (Figure S13) detected 10 μs and 50 μs after the laser pulse, a (delayed) emission around 600 nm is detectable. Although with these delay times the excited state of [Ru(phen)$_3$]$^{2+}$ should be essentially completely returned to the ground state, particularly in the presence of a quencher, the emission is very well detectable, especially at low concentration of PMS. This indicates a

back energy transfer from ^{3*}PMS to the sensitizer and consequently delayed emission from ^{3*}[Ru(phen)$_3$]$^{2+}$. The emission bands centered around 400 nm and 500 nm correspond to the (delayed) fluorescence and excimer emission of PMS (see also inset of Figure S14).[18]
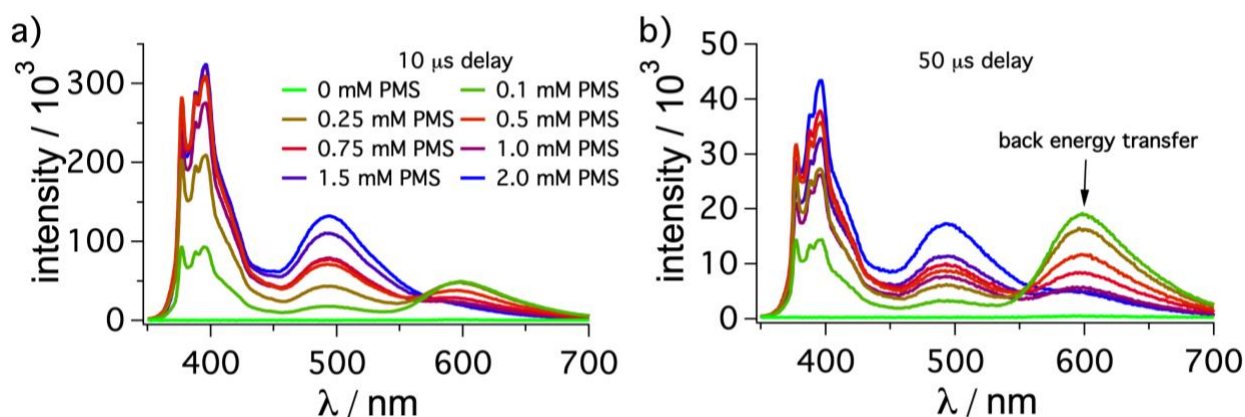
Figure S13. Time-resolved emission after sensitized ^{3*}PMS population. [Ru(phen)$_3$]$^{2+}$ (50 μM) in de-aerated DMF was excited at 532 nm in the presence of different concentrations of PMS and the emission spectra were recorded 10 μs (a) and 50 μs (b) after the laser pulse. All emission spectra are time-integrated over 2 μs.
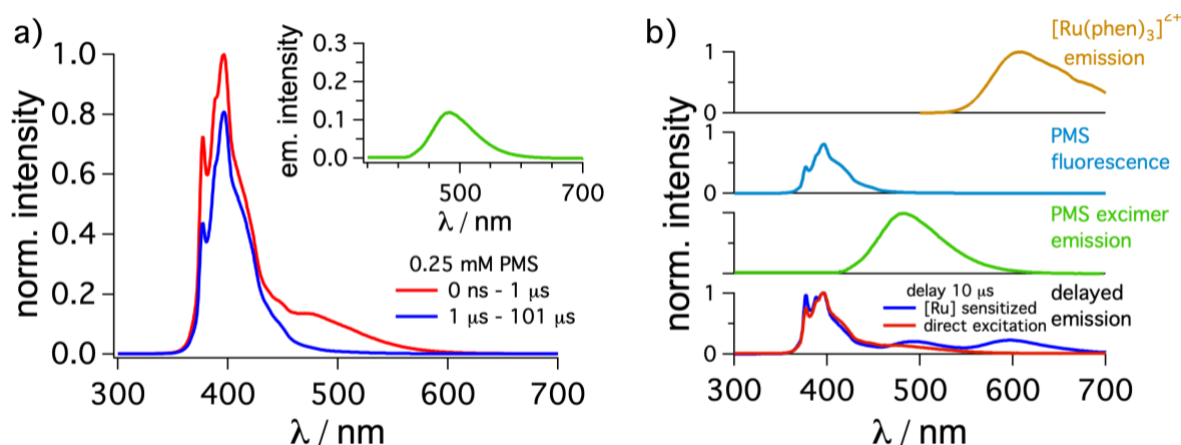
Figure S14. Time-resolved emission after direct and sensitized PMS excitation. PMS (250 μM) in de-aerated DMF was excited at 355 nm and the emission spectra were recorded over the first microsecond (red spectrum, promt emission) and the following 100 μs (blue spectrum, delayed emission). The excimer spectrum (solid green trace) based on the substraction between scaled spectra of the promt and delayed emission in (a) is presented as inset. b) Comparison of the emission of [Ru(phen)$_3$]$^{2+}$ (ocher, taken from Figure S5), fluorescence (pale blue, taken from blue trace in a) and excimer emission of PMS (green, taken from inset in a), as well as [Ru(phen)$_3$]$^{2+}$-sensitized delayed emission (blue spectrum, details in Figure S13) and delayed emission by direct excitation at 355 nm (red spectrum). In the bottom panel, the PMS concentration (250 μM), the time delay after the laser pulse (10 μs) and the integration time (2 μs) are identical for both spectra.

The clearly detectable excimer emission in the delayed emission spectrum even at low concentrations of PMS (e.g. 250 μM as ocher spectrum in Figure S13) implies that the triplet state rather than a singlet state is

predominantly responsible for the excimer emission. Assuming a diffusion-limited reaction between singlet-excited PMS and PMS in its ground state in DMF ($7.6 \cdot 10^9$ $M^{-1}s^{-1}$) and taking the (prompt) fluorescence lifetime of 6.7 ns (Table S1) less than 2 % of self-quenching is expected from the singlet state. The actual contribution of diffusion-mediated self-quenching is regarded to be even lower as the reaction between two anions is expected to be below 10^9 M^{-1} s^{-1}. Indeed, a time-resolved detection of the emission spectra (Figure S14a)[18] indicates only contributions from excimer emission (around 500 nm) in delayed emission (red trace). A comparison of the different delayed emission spectra detected – caused by $[Ru(phen)_3]^{2+}$-sensitized $^{3*}PMS$ population and population *via* intersystem crossing after direct excitation (Figure S14) – clearly highlight the back-energy transfer to $^{3*}[Ru(phen)_3]^{2+}$. Possibly even slightly enhanced excimer contributions for sensitized PMS emission caused by the locally higher concentration of negatively charged PMS around the positively charged sensitizer might be assumed based on the data sets. However, to understand these details much more comprehensive analyses would be needed,[19] and this is beyond the scope of this manuscript. Furthermore, these contributions as deactivation channel in our mediated upconversion system are likely very small due to the fast deactivation of $^{3*}PMS$ by DPA (section 4.2.6).
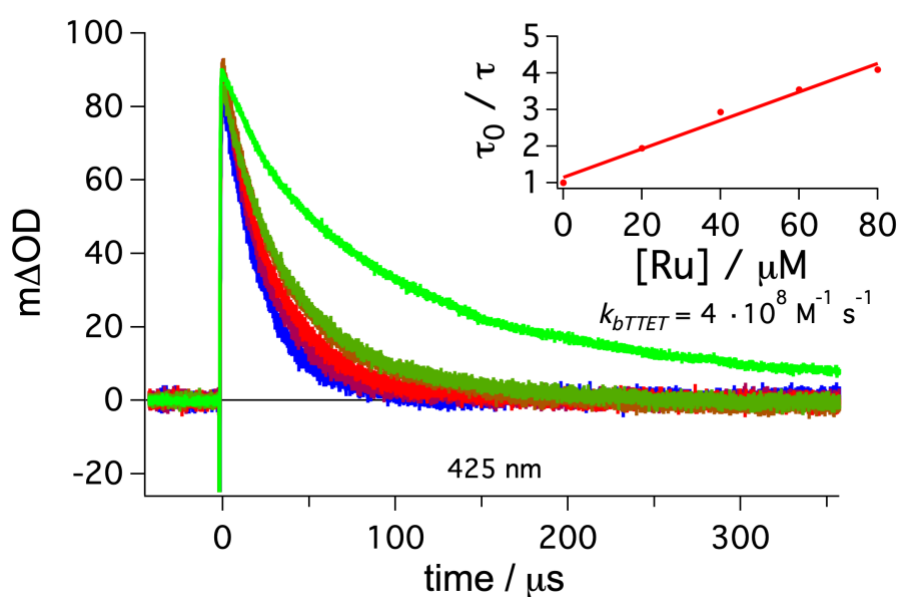
Figure S15. Decay curves of $^{3*}PMS$ in the presence of different concentrations of $[Ru(phen)_3]^{2+}$. PMS (150 μM) and $[Ru(phen)_3]^{2+}$ in de-aerated dimethylformamide were excited at 355 nm and the transient absorption decay was monitored at 425 nm in the absence (green) and in the presence of different concentrations of $[Ru(phen)_3]^{2+}$ (20, 40, 60, 80 μM). The Stern–Volmer plot obtained for the averaged lifetimes from the multiexponential decay pathway and the resulting quenching rate constant are given in the inset.

To analyze the back energy transfer in a Stern–Volmer-like analysis, a sensitized population of $^{3*}PMS$ will likely result in very divergent signal intensities complicating the analysis. As alternative pathway a direct excitation and intersystem crossing is possible to populate $^{3*}PMS$. A partial contribution for the excitation of

$[Ru(phen)_3]^{2+}$ is balanced by a change of the laser excitation intensity to result in similar maximum intensities at the absorption maximum of $^{3*}PMS$ (425 nm, for the transient absorption spectrum see also Figure S32). In principle a coupled equilibrium with different decay pathways is present in solution, but a detailed analysis is not straightforward in such a complex system. Qualitatively the datasets follow the expected trend for an equilibrium with a large change in the beginning (bright green *vs* dark green trace in Figure S15) and smaller changes with increasing concentrations of $[Ru(phen)_3](PF_6)_2$. For an estimation of the rate constant, the decay curves are fitted with a biexponential decay function and a rate constant of $\sim 4 \cdot 10^8$ M^{-1} s^{-1} is estimated. The Stern–Volmer plot (inset Figure S15) has some deviation from a linear behavior and this implies a more complicated overall deactivation pathway than it is depicted in the corresponding fit here. However, the estimated rate constant for back energy transfer is one order of magnitude smaller than the reverted process for the population of $^{3*}PMS$ ($9.2 \cdot 10^9$ M^{-1} s^{-1}) and this seems reasonable based on detectable delayed emission of $^{3*}[Ru(phen)_3]^{2+}$ in pulsed laser experiments (Figure S13), the triplet energies from 77K experiments, and diminished energy transfer rate constants determined by steady state spectroscopy in comparison to time-resolved spectroscopy (Table S3). The increaing noise of the curves with higher concentrations of $[Ru(phen)_3](PF_6)_2$ in Figure S15 is caused by increasing ground state absorption of the ruthenium sensitizer at the detection wavelength of 425 nm.

4.2.6. Stepwise triplet-triplet energy transfer from $^{3*}[Ru(phen)_3]^{2+}$ *via* PMS to DPA

The datasets presented in this section complement the measurements presented and discussed in Figure 3 of the main manuscript.
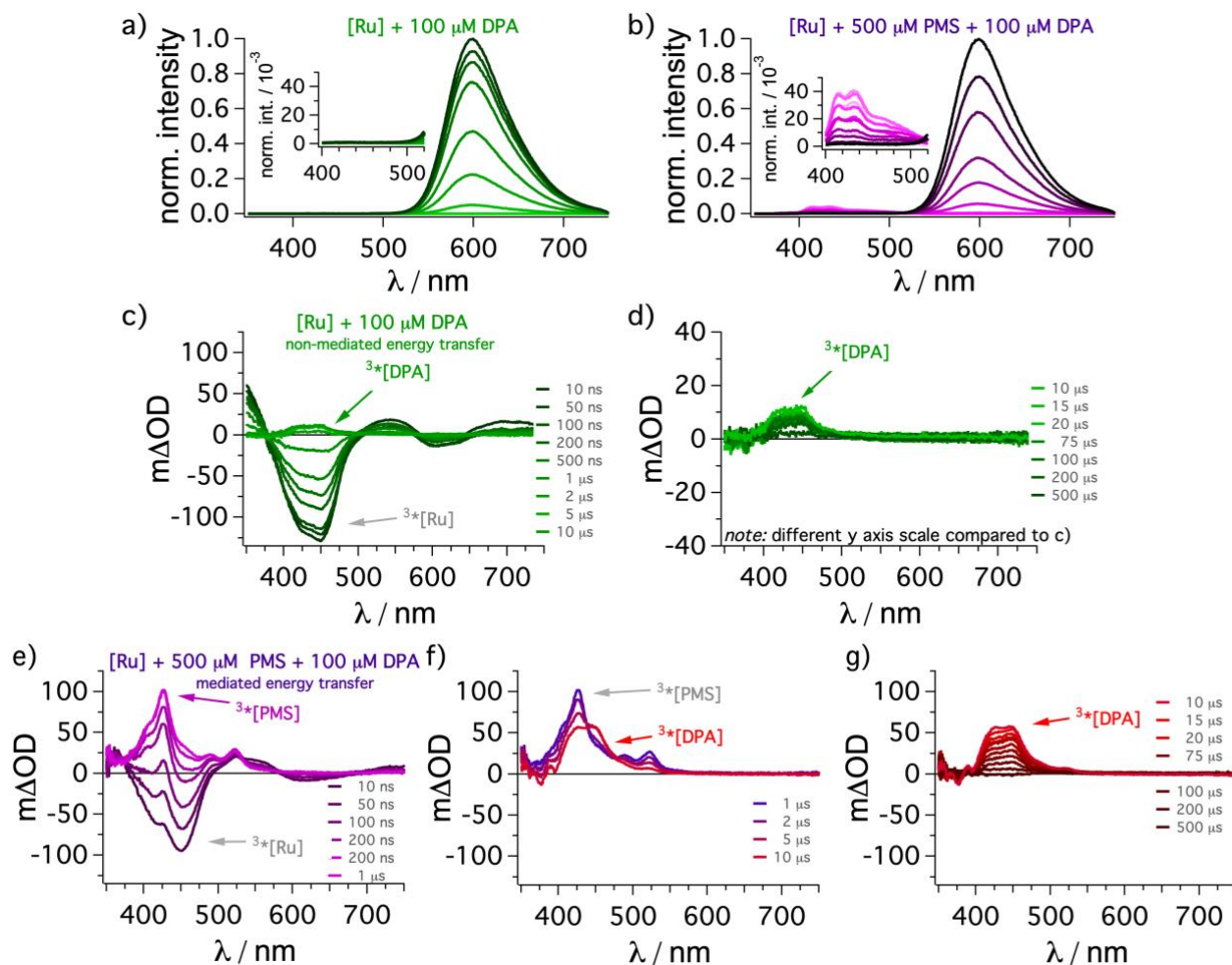
Figure S16. Time-resolved emission and transient absorption for the stepwise energy transfer cascade. $[Ru(phen)_3]^{2+}$ (50 μM) in de-aerated DMF was excited at 532 nm in the presence of DPA (100 μM) and the emission spectra after different time delays time-integrated over 50 ns were recorded in the absence (a) and presence (b) of PMS (500 μM). The transient absorption spectra with different time delays after the laser pulse of the same solution as in (a) is presented and separated to the time delays mainly for the formation of ^{3*}DPA (in panel c) and the decay thereof (in panel d). The transient absorption spectra with different time delays after the laser pulse of the same solution as in (b) is presented and separated to the time delays for the formation of ^{3*}PMA (in panel e), the second energy transfer to ^{3*}DPA (in panel f) and the decay thereof (in panel g). All transient absorption datasets are time-integrated over 50 ns and the detection delay times are indicated as insets.

The general discussion for the datasets in Figure S16c-g is provided in the main manuscript during the discussion of Figure 3. In the additional time-resolved emission measurements presented in Figure S16, the faster energy transfer from to $^{3*}[Ru(phen)_3]^{2+}$ to PMS (0.5 mM) compared to DPA (0.1 mM) is clearly seen (main part of Figure S16 a+b). Only in the mediated system significant delayed emission from DPA is visible

(insets of Figure S16 a+b), which is in line with a higher ^{3*}DPA concentration in this case. The summarized transient absorption traces of Figure 3 of the main manuscript are here presented again, but separated to the two (c-d) or three (e-g) steps occurring for the formation and decay of ^{3*}DPA. The transient absorption spectra in the presence of PMS clearly show the stepwise process for the formation of ^{3*}PMS (Figure S16e), subsequent energy transfer to ^{3*}DPA (Figure S16f) and the decay thereof (Figure S16g). In contrast, in the absence of mediator only the formation of ^{3*}DPA (Figure S16e) and the decay (Figure S16d) is visible. Consequently, as also pointed out in the main manuscript, the concentration of ^{3*}DPA is much higher in the presence of PMS compared to the direct energy transfer from ^{3*}[Ru(phen)$_3$]$^{2+}$ to DPA.

4.2.7. Triplet-triplet energy transfer from ^{3*}[Ru(phen)$_3$]$^{2+}$ to PMS in the presence of DPA

In the presence of 100 μM of DPA, the lifetime of ^{3*}PMS is expected to be much shorter compared to the excited state lifetime in the absence of annihilator (see also section 4.3). As a consequence, the measured steady-state and time-resolved quenching constants for the energy transfer from ^{3*}[Ru(phen)$_3$]$^{2+}$ to PMS are expected to get closer due to the diminished back energy transfer. Indeed, while the time-resolved quenching constant k_{TTET} (Figure S17) is similar to the data without DPA present ($9.1 \cdot 10^9$ M^{-1} s^{-1}), the bimolecular rate constant measured steady-state spectroscopy is significantly higher ($7.8 \cdot 10^9$ M^{-1} s^{-1}, Figure S18) compared to the value in the absence of DPA ($6.1 \cdot 10^9$ M^{-1} s^{-1}).
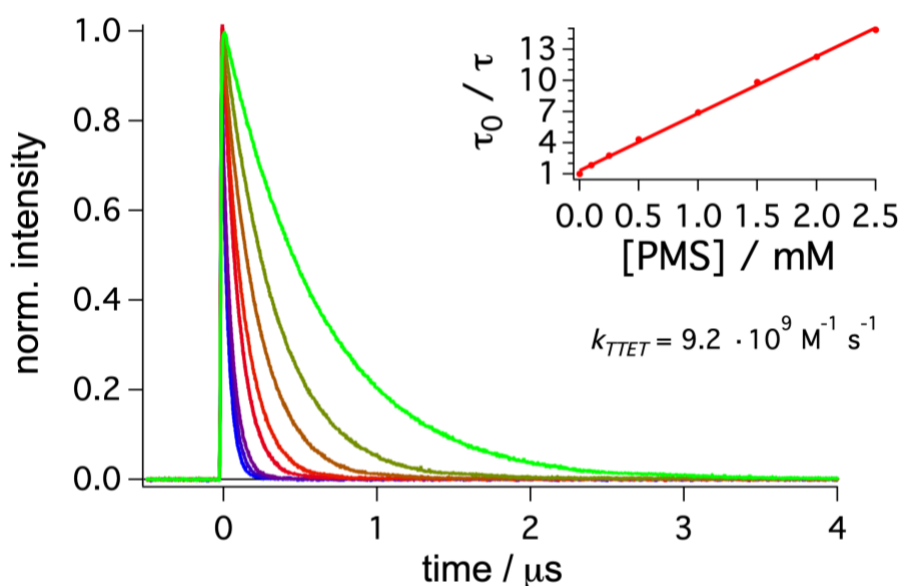
Figure S17. Emission lifetime quenching of ^{3*}[Ru(phen)$_3$]$^{2+}$ by **PMS** in the presence of DPA (100 μM). [Ru(phen)$_3$]$^{2+}$ (50 μM) in de-aerated dimethylformamide was excited at 532 nm and the emission decay was monitored at 600 nm in the absence (green) and in the presence of different concentrations of PMS (0.05, 0.10, 0.25, 0.5, 0.75, 1.0, 1.5 mM). The Stern−Volmer plot obtained from this data set and and the resulting quenching rate constant are given in the inset.

Figure S18. Steady-state emission quenching of ^{3*}[Ru(phen)$_3$]$^{2+}$ by **PMS** in the presence of DPA (100 μM). [Ru(phen)$_3$]$^{2+}$ (50 μM) in de-aerated dimethylformamide was excited at 490 nm and the emission was monitored in the absence (green) and in the presence of different concentrations of PMS (0.1, 0.25, 0.5, 1.0, 1.5, 2.0, 2.5 mM). The Stern−Volmer plot obtained from this data set and and the resulting quenching rate constant (with τ_0 taken from Figure S17) are given in the inset.

4.2.8. Triplet-triplet energy transfer from ^{3*}[Ru(phen)$_3$]$^{2+}$ to Py
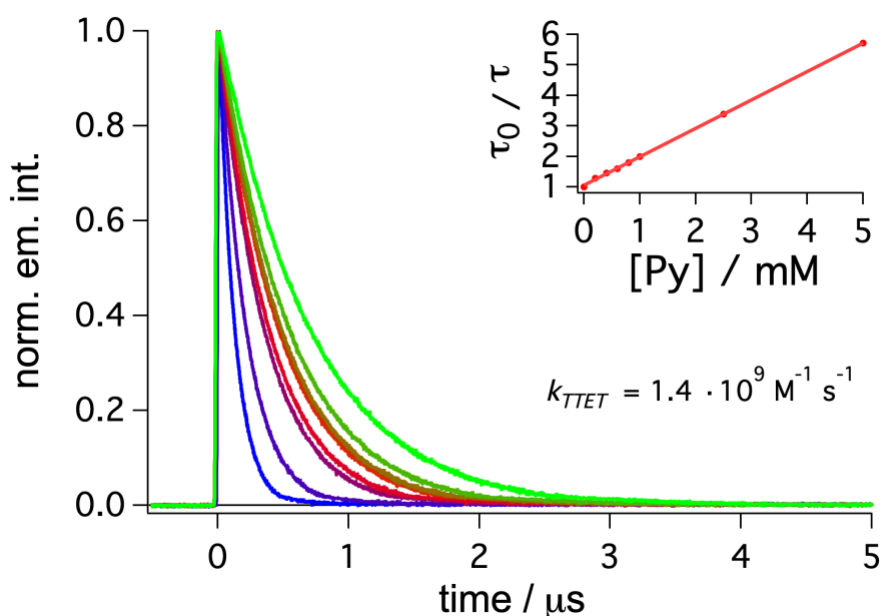
Figure S19. Emission lifetime quenching of ^{3*}[Ru(phen)$_3$]$^{2+}$ by **Py**. [Ru(phen)$_3$]$^{2+}$ (50 μM) in de-aerated dimethylformamide was excited at 532 nm and the emission decay was monitored at 600 nm in the absence (green) and in the presence of different concentrations of Py (0.1, 0.2, 0.4, 0.6, 0.8, 1, 2.5, 5 mM). The Stern−Volmer plot obtained from this data set and and the resulting quenching rate constant are given in the inset.
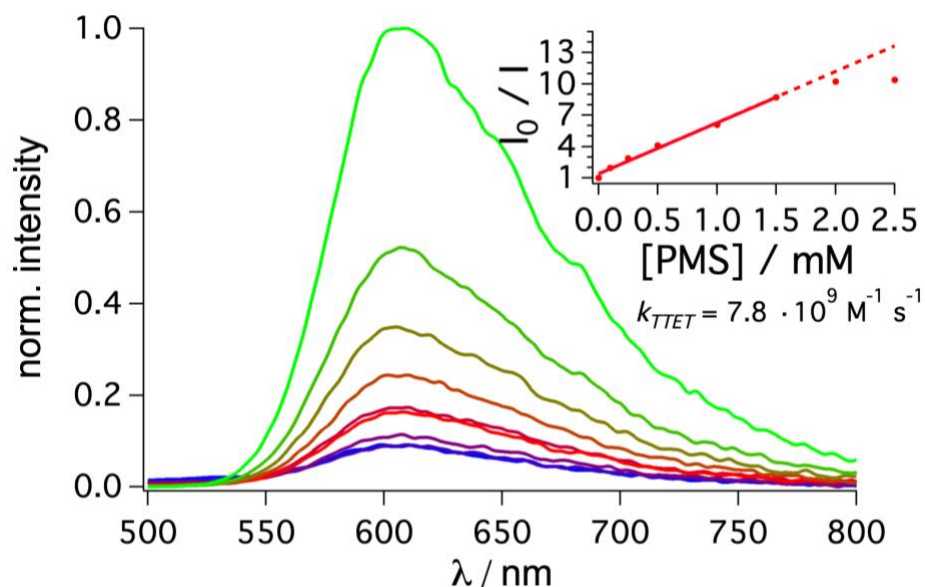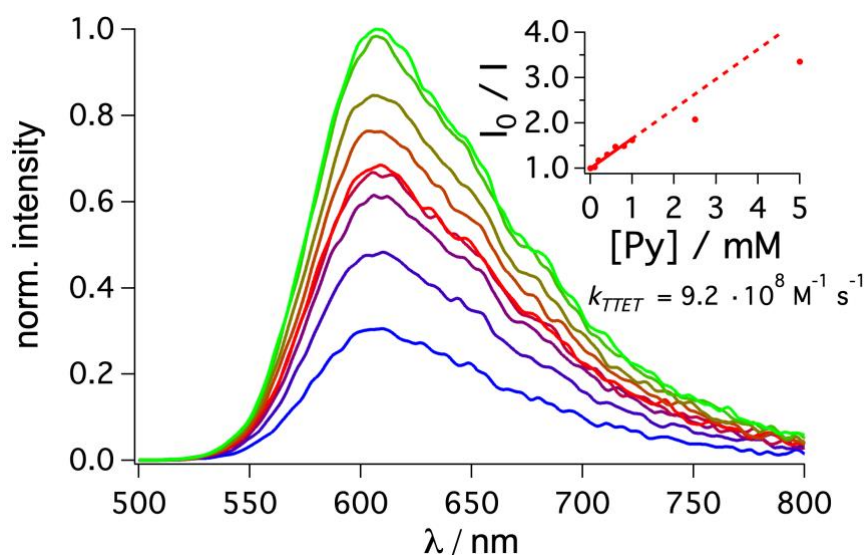
Figure S20. Steady-state emission quenching of $^{3*}[Ru(phen)_3]^{2+}$ by **Py**. $[Ru(phen)_3]^{2+}$ (50 μM) in de-aerated dimethylformamide was excited at 490 nm and the emission was monitored in the absence (green) and in the presence of different concentrations of Py (0.1, 0.2, 0.4, 0.6, 0.8, 1, 2.5, 5 mM). The Stern–Volmer plot obtained from this data set and and the resulting quenching rate constant (with τ_0 taken from Figure S18) are given in the inset.
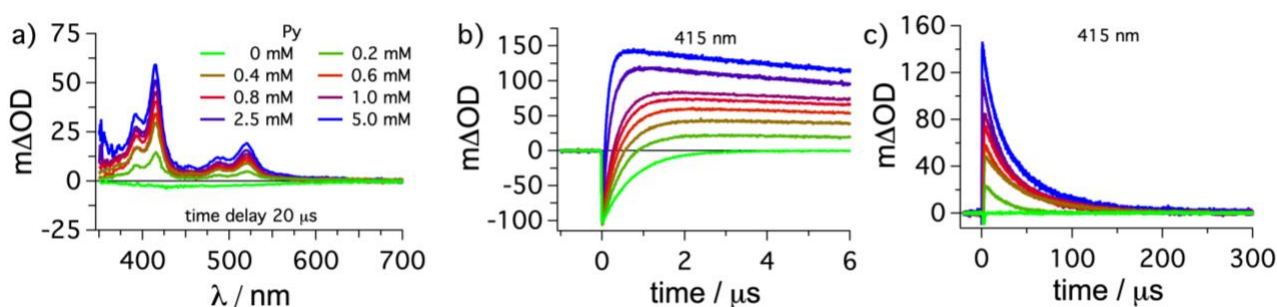
Figure S21. Time-resolved transient absorption following the formation and decay of ^{3*}Py in the reference system. a) $[Ru(phen)_3]^{2+}$ (50 μM) in de-aerated DMF was excited at 532 nm in the presence of different concentrations of Py and the transient absorption spectra, time-integrated over 200 ns, were recorded 20 μs after the laser pulse. The kinetic transient absoprtion traces for the formation on a short μs time scale (b) and over 300 μs from the same solutions was detected at 415 nm. The color code for all figure parts is provided in panel (a).

The transient absorption spectra (Figure S21a) measured with a time delay of 20 μs after the laser pulse of a solution of 50 μM $[Ru(phen)_3](PF_6)_2$ in de-aerated DMF in the presence of Py contains the characteristic spectral features of ^{3*}Py.[20] With higher concentrations of pyrene, the concentrations of ^{3*}Py increase and the ^{3*}Py formation is faster (Figure S21b), as expected from the Stern–Volmer measurements (Figure S19). The ^{3*}Py decay (Figure S21c) is on a similar time scale as the decay of ^{3*}PMS and a use as uncharged reference compound is reasonable. These measurements are in line with literature data with $[Ru(bpy)_3](PF_6)_2$ in DMSO as solvent.[21]

4.2.9. Overview: triplet-triplet energy transfer from other sensitizers

Further information concerning the rate constant <u>with differently charged sensitizers</u> is given here.

Table S4. Summary of relevant data and energy transfer rate constants with other sensitizers. [a]

catalyst	quencher	k / M^{-1} s^{-1} [b]	k / M^{-1} s^{-1} [c]	Figure
$[Ru(phen)_3]^{2+}$	PMS	$9.1 \cdot 10^9$	$6.1 \cdot 10^9$	Figure S9 Figure S8
$[Ru(phen)_3]^{2+}$	Py	$1.4 \cdot 10^9$	$9.2 \cdot 10^8$	Figure S20 Figure S19
$[Ir(dFbpyCF_3)_2(bpy)]^+$	PMS	$5.7 \cdot 10^9$	$4.9 \cdot 10^9$	Figure S23 Figure S22
$[Ir(dFbpyCF_3)_2(bpy)]^+$	Py	$3.4 \cdot 10^9$	$2.8 \cdot 10^9$	Figure S27 Figure S26
$[Ir(ppy)_3]$	PMS	$2.5 \cdot 10^9$	$2.5 \cdot 10^9$	Figure S25 Figure S24
$[Ir(ppy)_3]$	Py	$3.5 \cdot 10^9$	$3.8 \cdot 10^9$	Figure S29 Figure S28

a) The unquenched excited state lifetimes (τ_0) of $[Ir(dFbpyCF_3)_2(bpy)]^+$ and $[Ir(ppy)_3]$ in dimethylformamide are 1700 µs and 1460 ns, respectively. b) Time-resolved measurements. c) Steady-state measurements.

4.2.10. Triplet-triplet energy transfer from ^{3*}[Ir(dFbpyCF$_3$)(bpy)]$^+$ to PMS
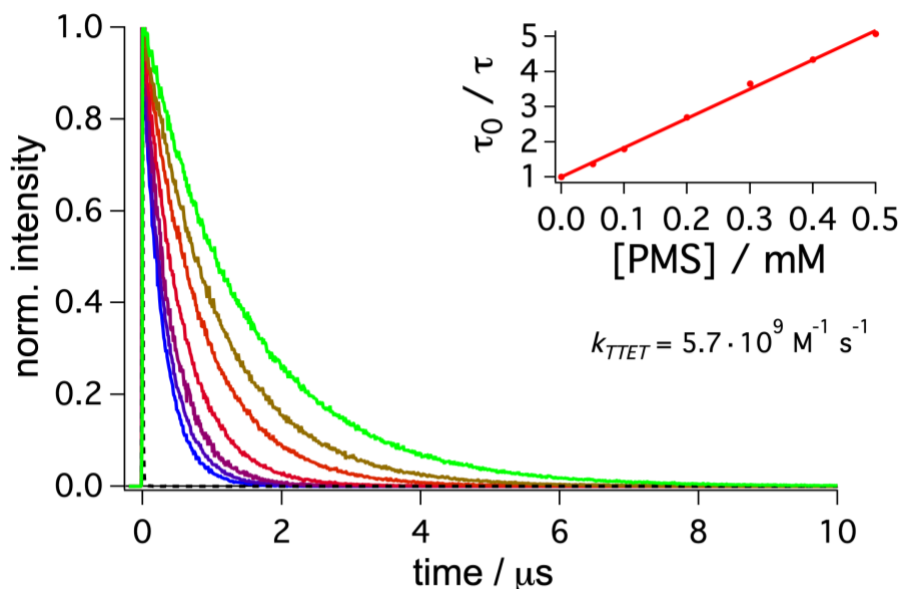
Figure S22. Emission lifetime quenching of ^{3*}**[Ir(dFbpyCF$_3$)(bpy)]$^+$** by **PMS**. [Ir(dFbpyCF$_3$)(bpy)]$^+$ (50 μM) in de-aerated dimethylformamide was excited at 450 nm and the emission decay (TCSPC technique) was monitored with a 500 nm bandpass filter (±25 nm) in the absence (green) and in the presence of different concentrations of PMS (0.05, 0.1, 0.2, 0.3, 0.4, 0.5 mM). The instrument response function (IRF) is provided as black dotted line. The Stern−Volmer plot obtained from this data set and and the resulting quenching rate constant are given in the inset.

Figure S23. Steady-state emission quenching of ^{3*}**[Ir(dFbpyCF$_3$)(bpy)]$^+$** by **PMS**. [Ir(dFbpyCF$_3$)(bpy)]$^+$ (50 μM) in de-aerated dimethylformamide was excited at 430 nm and the emission was monitored in the absence (green) and in the presence of different concentrations of PMS (0.05, 0.1, 0.2, 0.3, 0.4, 0.5 mM). The Stern−Volmer plot obtained from this data set and and the resulting quenching rate constant (with τ_0 taken from Figure S22) are given in the inset.

4.2.11. Triplet-triplet energy transfer from ^{3*}[Ir(ppy)$_3$] to PMS
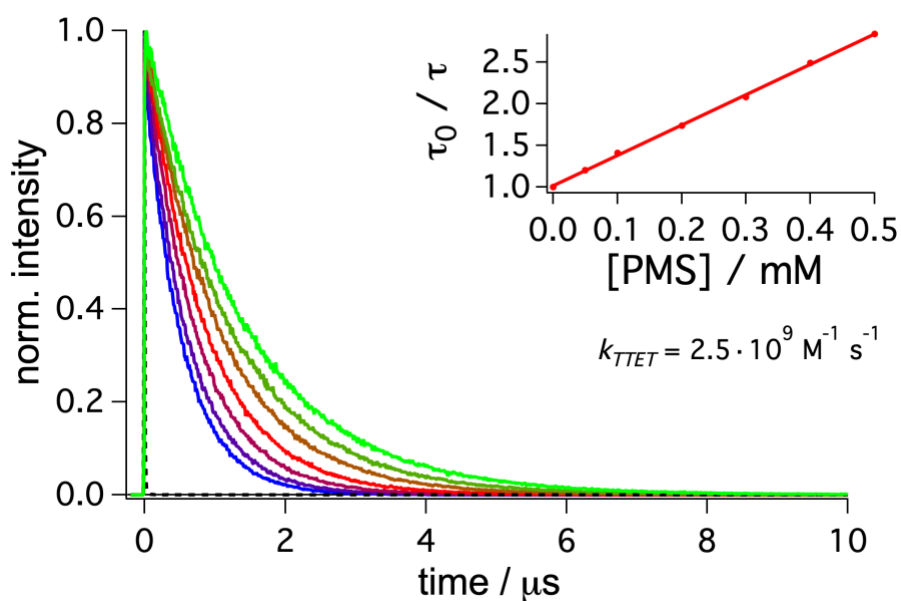
Figure S24. Emission lifetime quenching of ^{3*}**[Ir(ppy)$_3$]** by **PMS**. [Ir(ppy)$_3$] (30 µM) in de-aerated dimethylformamide was excited at 450 nm and the emission decay was monitored with a 500 nm bandpass filter (±25 nm) in the absence (green) and in the presence of different concentrations of PMS (0.05, 0.1, 0.2, 0.3, 0.4, 0.5 mM). The instrument response function (IRF) is provided as black dotted line. The Stern–Volmer plot obtained from this data set and and the resulting quenching rate constant are given in the inset.

Figure S25. Steady-state emission quenching of ^{3*}**[Ir(ppy)$_3$]** by **PMS**. [Ir(ppy)$_3$] (30 µM) in de-aerated dimethylformamide was excited at 450 nm and the emission was monitored in the absence (green) and in the presence of different concentrations of PMS (0.05, 0.1, 0.2, 0.3, 0.4, 0.5 mM). The Stern–Volmer plot obtained from this data set and and the resulting quenching rate constant (with τ_0 taken from Figure S24) are given in the inset.
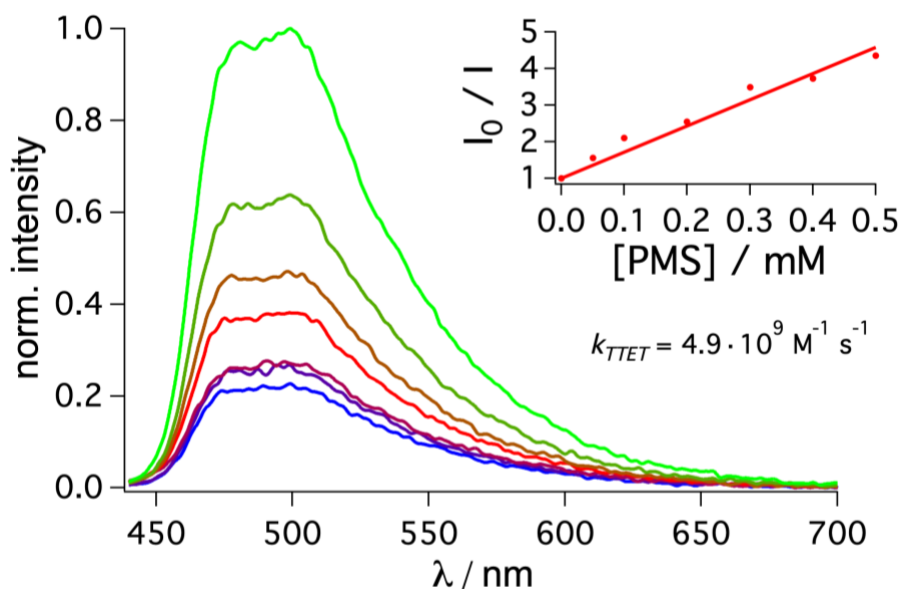
4.2.12. Triplet-triplet energy transfer from $^{3*}[Ir(dFbpyCF_3)(bpy)]^+$ to Py
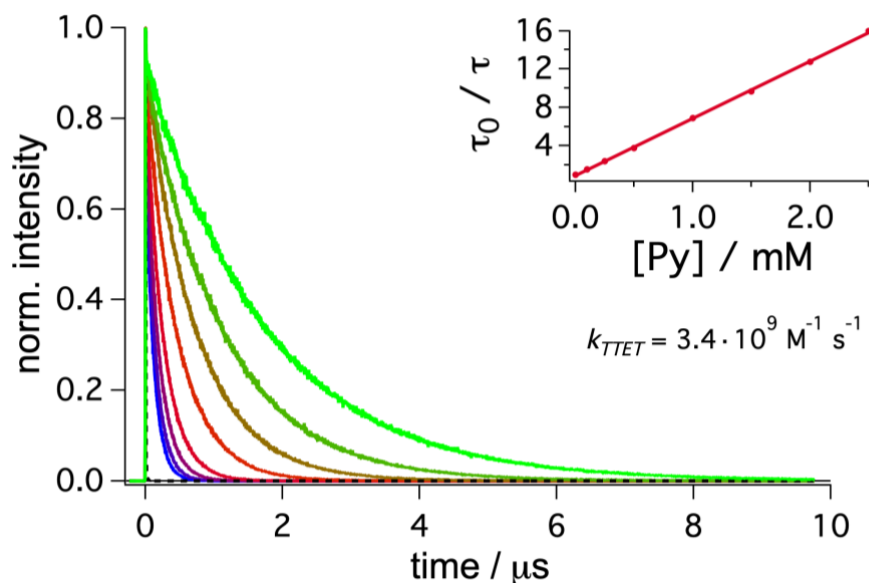
Figure S26. Emission lifetime quenching of ^{3*}**[Ir(dFbpyCF₃)(bpy)]⁺** by **Py.** [Ir(dFbpyCF₃)(bpy)]⁺ (50 μM) in de-aerated dimethylformamide was excited at 450 nm and the emission decay was monitored with a 500 nm bandpass filter (±25 nm) in the absence (green) and in the presence of different concentrations of Py (0.05, 0.1, 0.25, 0.5, 1.0, 1.5, 2.0, 2.5 mM). The instrument response function (IRF) is provided as black dotted line. The Stern−Volmer plot obtained from this data set and and the resulting quenching rate constant are given in the inset.
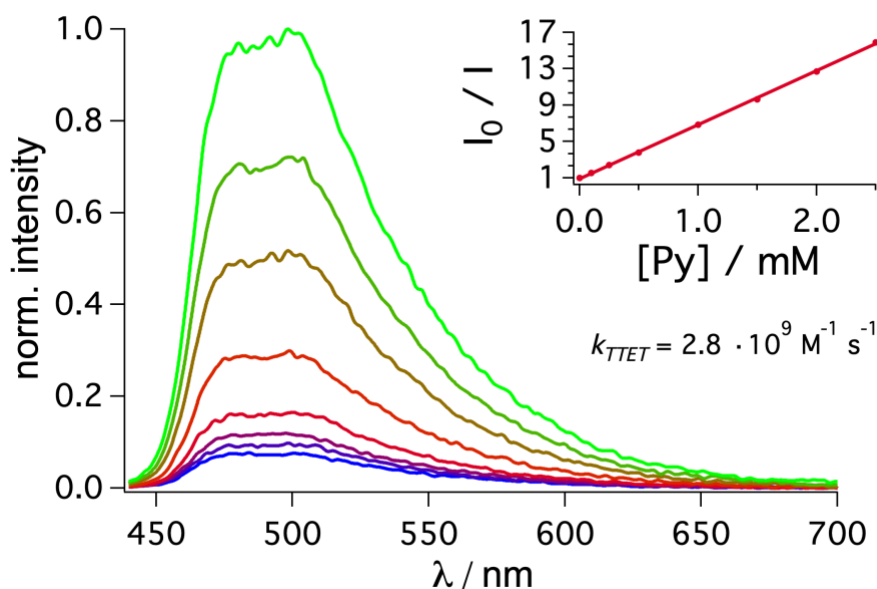
Figure S27. Steady-state emission quenching of ^{3*}**[Ir(dFbpyCF₃)(bpy)]⁺** by **Py.** [Ir(dFbpyCF₃)(bpy)]⁺ (50 μM) in de-aerated dimethylformamide was excited at 430 nm and the emission was monitored in the absence (green) and in the presence of different concentrations of Py (0.05, 0.1, 0.25, 0.5, 1.0, 1.5, 2.0, 2.5 mM). The Stern−Volmer plot obtained from this data set and and the resulting quenching rate constant (with τ_0 taken from Figure S28) are given in the inset.

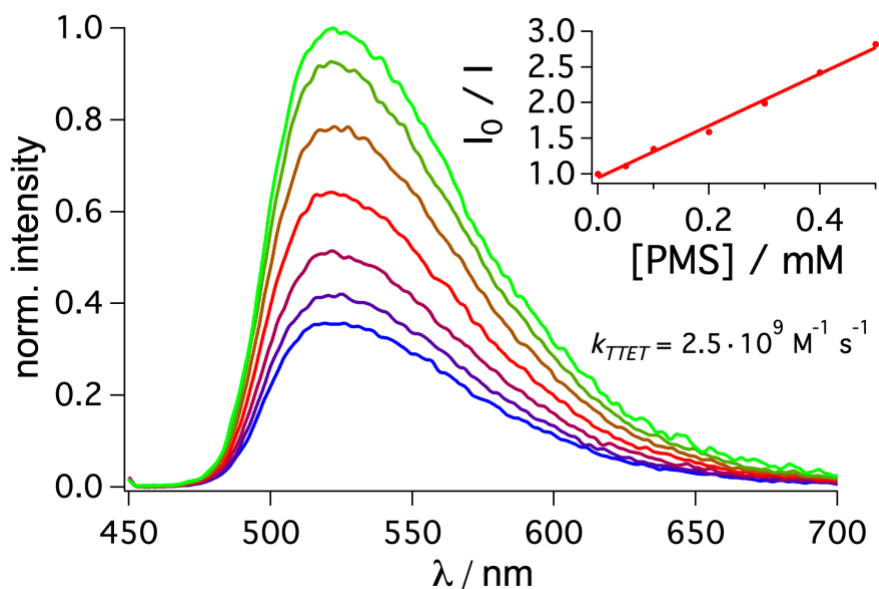## 4.2.13. Triplet-triplet energy transfer from ^{3*}[Ir(ppy)$_3$] to Py
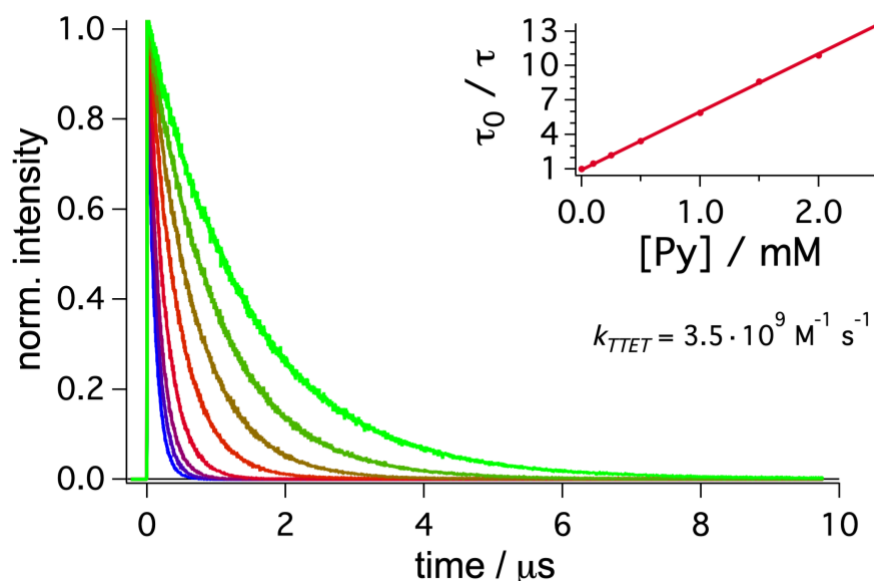
Figure S28. Emission lifetime quenching of ^{3*}**[Ir(ppy)₃]** by **Py.** [Ir(ppy)₃] (50 μM) in de-aerated dimethylformamide was excited at 450 nm and the emission decay was monitored with a 500 nm bandpass filter (±25 nm) in the absence (green) and in the presence of different concentrations of Py (0.05, 0.1, 0.25, 0.5, 1.0, 1.5, 2.0, 2.5 mM). The instrument response function (IRF) is provided as black dotted line. The Stern−Volmer plot obtained from this data set and and the resulting quenching rate constant are given in the inset.

Figure S29. Steady-state emission quenching of ^{3*}**[Ir(ppy)₃]** by **Py.** [Ir(ppy)₃] (50 μM) in de-aerated dimethylformamide was excited at 450 nm and the emission was monitored in the absence (green) and in the presence of different concentrations of Py (0.05, 0.1, 0.25, 0.5, 1.0, 1.5, 2.0, 2.5 mM). The Stern−Volmer plot obtained from this data set and and the resulting quenching rate constant (with τ_0 taken from Figure S28) are given in the inset.

4.2.14. Overview: triplet-triplet energy transfer in the presence of additional salt

Further information concerning the rate constants <u>with ammonium hexafluorophosphate present as additional salt in higher concentration</u> is given here.

Table S5. Summary of relevant data and energy transfer rate constants with other sensitizers. [a]

catalyst	quencher	NH_4PF_6	k / M^{-1} s^{-1} [b]	k / M^{-1} s^{-1} [c]	Figure
$[Ru(phen)_3]^{2+}$	PMS	-	$9.1 \cdot 10^9$	$6.1 \cdot 10^9$	Figure S9 Figure S8
$[Ru(phen)_3]^{2+}$	PMS	20 mM	$2.6 \cdot 10^9$	$1.5 \cdot 10^9$	Figure S30 Figure S31
$[Ru(phen)_3]^{2+}$	Py	-	$1.4 \cdot 10^9$	$9.2 \cdot 10^8$	Figure S19 Figure S20
$[Ru(phen)_3]^{2+}$	Py	20 mM	$1.3 \cdot 10^9$	$8.1 \cdot 10^8$	Figure S33 Figure S34
$[Ru(phen)_3]^{2+}$	DPA		$2.0 \cdot 10^9$	$2.1 \cdot 10^9$	Figure S10 Figure S11
$[Ru(phen)_3]^{2+}$	DPA	20 mM	$1.6 \cdot 10^9$	$1.2 \cdot 10^9$	Figure S35 Figure S36

a) The unquenched excited state lifetime (τ_0) of $[Ru(phen)_3]^{2+}$ is presented in Table S1. b) Time-resolved measurements. c) Steady-state measurements.

4.2.15. Triplet-triplet energy transfer from $^{3*}[Ru(phen)_3]^{2+}$ to PMS in the presence of NH$_4$PF$_6$
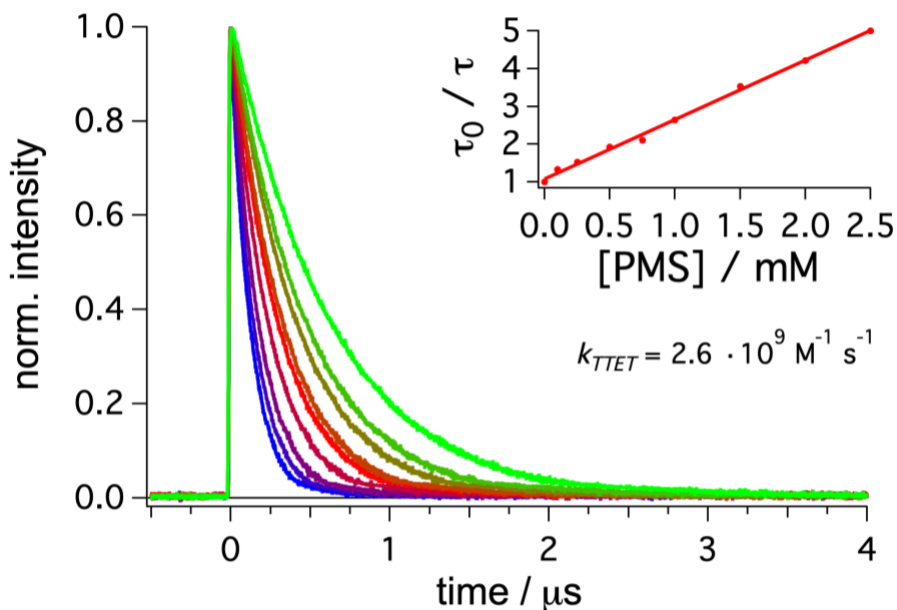
Figure S30. Emission lifetime quenching of $^{3*}[Ru(phen)_3]^{2+}$ by **PMS** in the presence of ammonium hexafluorophosphate (20 mM). $[Ru(phen)_3]^{2+}$ (50 μM) in de-aerated dimethylformamide with NH$_4$PF$_6$ (20 mM) in solution was excited at 532 nm and the emission decay was monitored at 600 nm in the absence (green) and in the presence of different concentrations of PMS (0.05, 0.10, 0.25, 0.5, 0.75, 1.0, 1.5 mM). The Stern−Volmer plot obtained from this data set and and the resulting quenching rate constant are given in the inset.

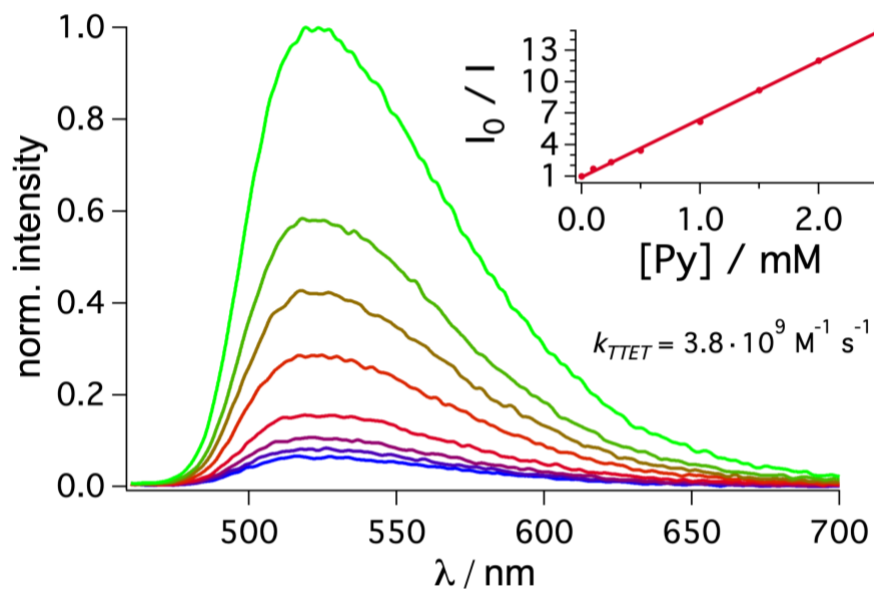**Figure S31.** Steady-state emission quenching of $^{3*}[Ru(phen)_3]^{2+}$ by **PMS** in the presence of ammonium hexafluorophosphate (20 mM). $[Ru(phen)_3]^{2+}$ (50 μM) in de-aerated dimethylformamide with NH$_4$PF$_6$ (20 mM) in solution was excited at 490 nm and the emission was monitored in the absence (green) and in the presence of different concentrations of PMS (0.1, 0.25, 0.5, 0.75, 1.0, 1.5 mM). The Stern−Volmer plot obtained from this data set and and the resulting quenching rate constant (with τ$_0$ taken from Figure S30) are given in the inset.
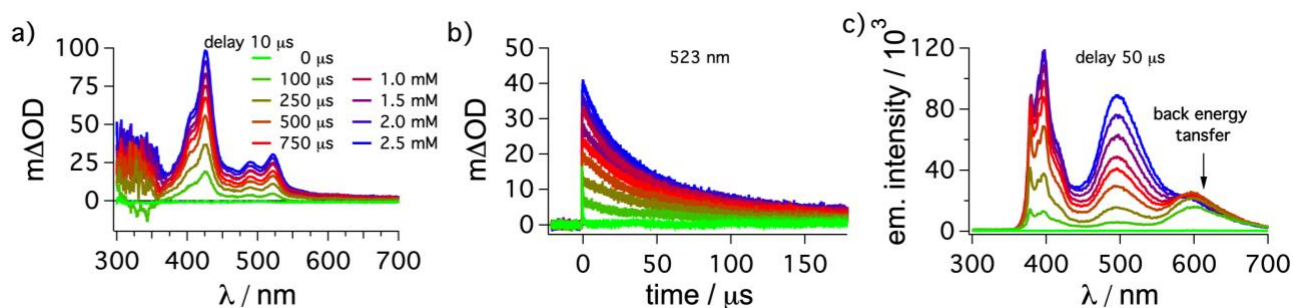
Figure S32. Time-resolved transient absorption spectroscopy. a) $[Ru(phen)_3]^{2+}$ (50 μM) in de-aerated DMF containing 20 mM NH_4PF_6 was excited at 532 nm in the presence of different concentrations of PMS and the transient absorption spectra, time-integrated over 200 ns, were recorded 10 μs after the laser pulse. b) The kinetic transient absoprtion traces following the decay of ^{3*}PMS of the same solution was monitored at 523 nm. c) Emission spectra 50 μs after the laser pulse, time-integrated over 2 μs. The color code for all figure parts is provided in panel (a).

As expected, while the energy transfer rate constants differ (Table S5) the shape of the ^{3*}PMS transient absorption spectra 10 μs after the laser pulse (and the emission spectra) are not influenced by the presence of ammonium hexafluorophosphate (compare Figure S13, Figure S16 and Figure S32).

### 4.2.16. Triplet-triplet energy transfer from $^{3*}[Ru(phen)_3]^{2+}$ to Py in the presence of NH_4PF_6
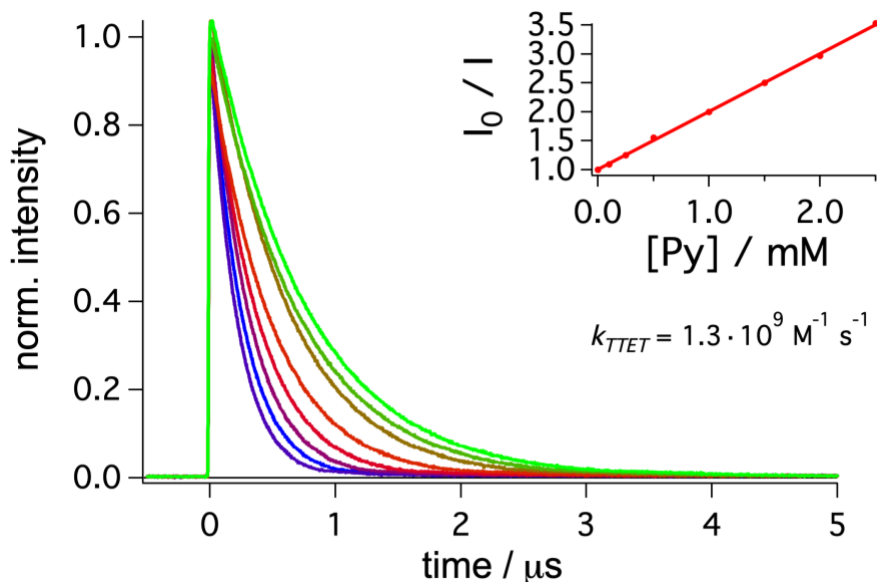
Figure S33. Emission lifetime quenching of $^{3*}[Ru(phen)_3]^{2+}$ by **Py** in the presence of ammonium hexafluorophosphate (20 mM). $[Ru(phen)_3]^{2+}$ (50 μM) in de-aerated dimethylformamide with NH_4PF_6 (20 mM) in solution was excited at 532 nm and the emission decay was monitored at 600 nm in the absence (green) and in the presence of different concentrations of Py (0.05, 0.10, 0.25, 0.5, 1.0, 1.5, 2.0, 2.5 mM). The Stern–Volmer plot obtained from this data set and and the resulting quenching rate constant are given in the inset.
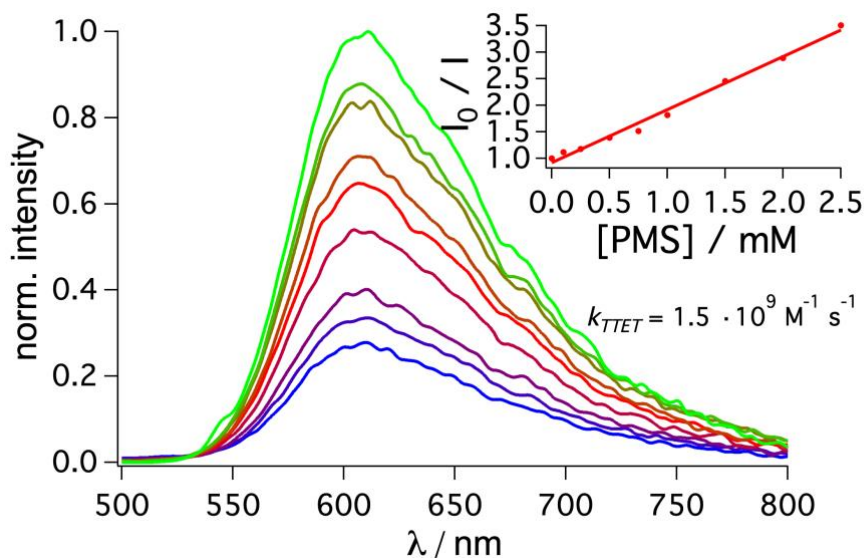
Figure S34. Steady-state emission quenching of ^{3*}[Ru(phen)$_3$]$^{2+}$ by **Py** in the presence of ammonium hexafluorophosphate (20 mM). [Ru(phen)$_3$]$^{2+}$ (50 µM) in de-aerated dimethylformamide with NH$_4$PF$_6$ (20 mM) in solution was excited at 490 nm and the emission was monitored in the absence (green) and in the presence of different concentrations of Py (0.1, 0.25, 0.5, 1.0, 1.5, 2.0, 2.5 mM). The Stern–Volmer plot obtained from this data set and and the resulting quenching rate constant (with τ_0 taken from Figure S33) are given in the inset.

4.2.17. Triplet-triplet energy transfer from ^{3*}[Ru(phen)$_3$]$^{2+}$ to DPA in the presence of NH$_4$PF$_6$
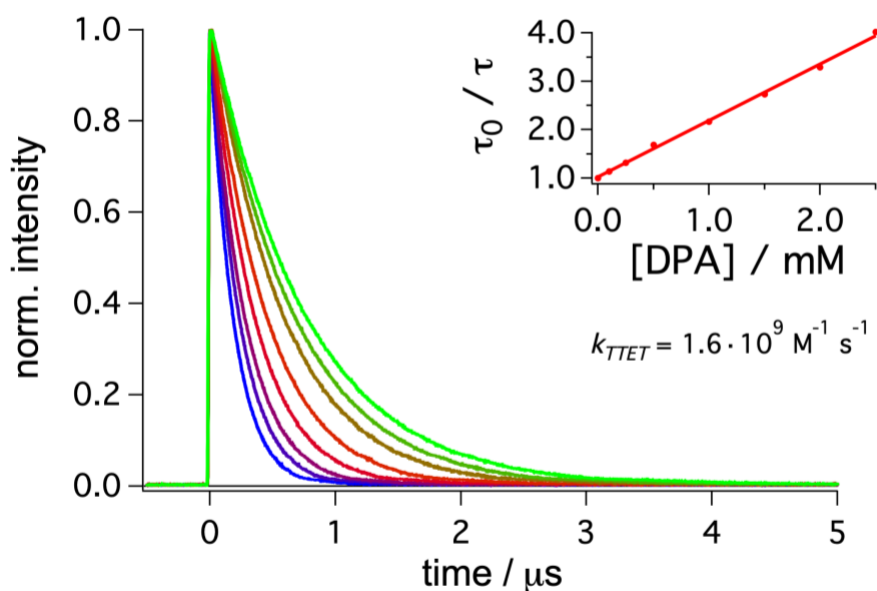
Figure S35. Emission lifetime quenching of ^{3*}[Ru(phen)$_3$]$^{2+}$ by **DPA** in the presence of ammonium hexafluorophosphate (20 mM). [Ru(phen)$_3$]$^{2+}$ (50 µM) in de-aerated dimethylformamide with NH$_4$PF$_6$ (20 mM) in solution was excited at 532 nm and the emission decay was monitored at 600 nm in the absence (green) and in the presence of different concentrations of DPA (0.05, 0.10, 0.25, 0.5, 1.0, 1.5, 2.0, 2.5 mM). The Stern–Volmer plot obtained from this data set and and the resulting quenching rate constant are given in the inset.
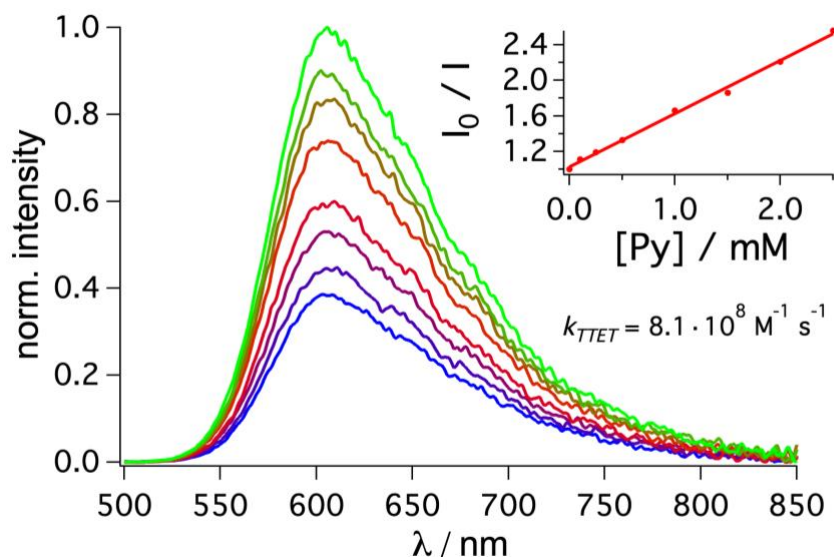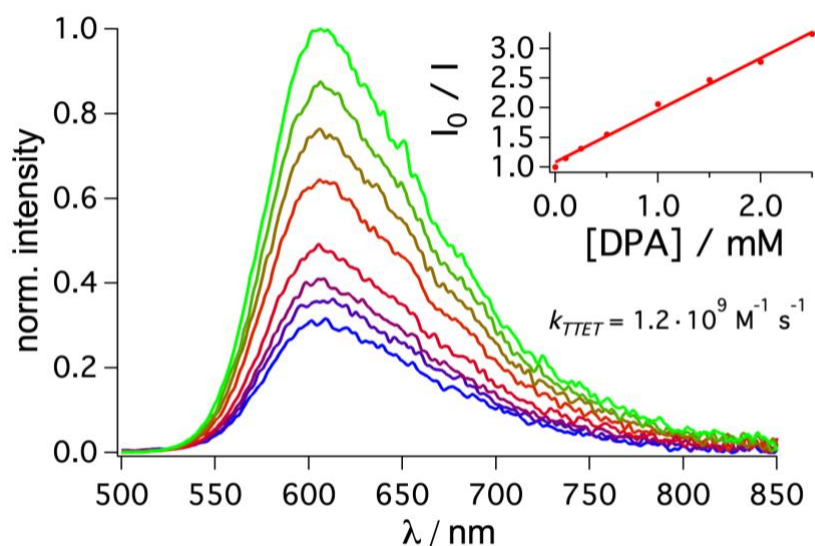
Figure S36. Steady-state emission quenching of ^{3*}[Ru(phen)$_3$]$^{2+}$ by **DPA** in the presence of ammonium hexafluorophosphate (20 mM). [Ru(phen)$_3$]$^{2+}$ (50 μM) in de-aerated dimethylformamide with NH$_4$PF$_6$ (20 mM) in solution was excited at 490 nm and the emission was monitored in the absence (green) and in the presence of different concentrations of DPA (0.1, 0.25, 0.5, 1.0, 1.5, 2.0, 2.5 mM). The Stern–Volmer plot obtained from this data set and and the resulting quenching rate constant (with τ_0 taken from Figure S35) are given in the inset.

4.3. Triplet-triplet energy transfer from ^{3*}PMS to DPA

Further information concerning the rate constant of <u>step 2</u> in Figure S7 is given here.
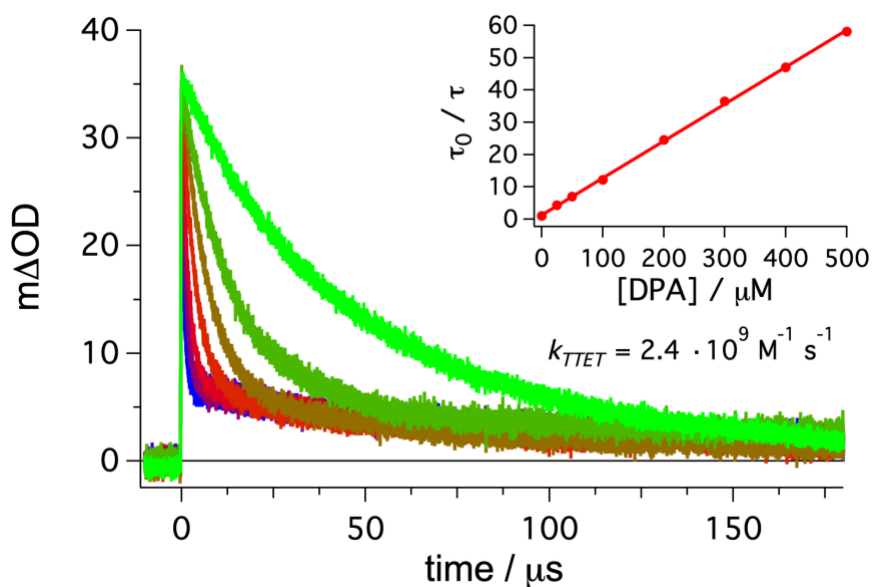
Figure S37. Excited state quenching of ^{3*}PMS by DPA. [Ru(phen)$_3$]$^{2+}$ (50 μM) in de-aerated dimethylformamide was excited at 532 nm in the presence of PMS (2.5 mM) and the transient absorption signal at 525 nm – corresponding to ^{3*}PMS – was monitored in the absence (green) and in the presence of different concentrations of DPA (25, 50, 100, 200, 300, 400, 500 μM). The Stern–Volmer plot obtained from this data set usng an initial lifetime τ_0 of 47 μs and and the resulting quenching rate constant are given in the inset. Further details are provided in the text.
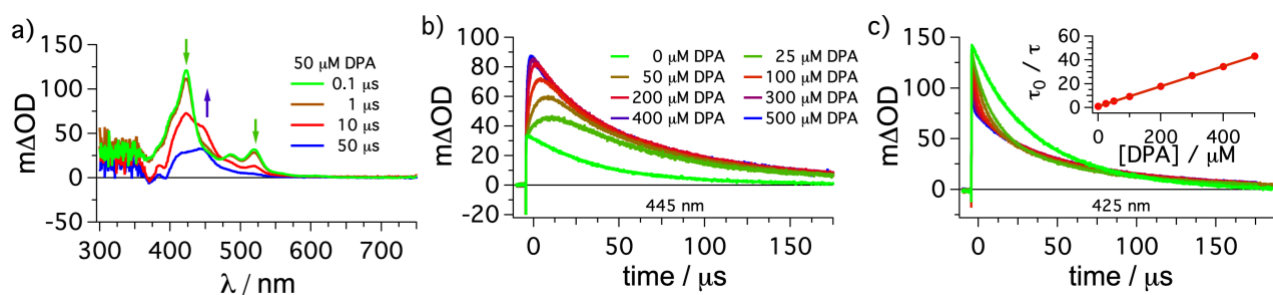
Figure S38. Transient absorption spectra and kinetic traces analyzing the energy transfer from ^{3*}PMS to DPA. a) Ru(phen)$_3$]$^{2+}$ (50 μM) in de-aerated dimethylformamide was excited at 532 nm in the presence of PMS (2.5 mM) and the transient absorption spectra with different time delay after the laser pulse were measured with DPA (50 μM). The kinetics of the transient absorption signal with different concentrations of DPA at 425 nm (b, maximum of ^{3*}PMS) and the maximum of the ^{3*}DPA signal at 445 nm (c, maximum of ^{3*}DPA) were measured over time. A Stern−Volmer plot based on the shorter componenet of a biexponential fit at 425 nm is presented as inset in (c). The color code for (a) as well as (b+c) is provided in the respective figure panel.

The transient absorption signal at 525 nm was monitored to analyze the second energy transfer step from ^{3*}PMS to DPA (Figure S37). After excitation of 50 μM [Ru(phen)$_3$]$^{2+}$ with a green laser pulse in the presence of 2.5 mM PMS a rapid formation of ^{3*}PMS with an absorption maximum at 425 nm is detected.[18] Different excited state deactivation pathways including back energy transfer from ^{3*}PMS to [Ru(phen)$_3$]$^{2+}$ (section 4.2.5) and triplet-triplet annihilation between two ^{3*}PMS as well as radiationless deactivation to the ground state are possible here. This situation would in principle require a combination of mono- and biexponential fit components to receive an accurate value for the triplet state lifetime of PMS in the absence and presence of DPA. Unfortunaly, there is a significant overlap between the triplet spectum of ^{3*}PMS and ^{3*}DPA and a clean observation of the triplet of PMS is not possible in the presence of new spectroscopic features of ^{3*}DPA (Figure S38a). Hence, for all measurements with DPA present, the decay is fitted with a biexponential fit function. In the transient absorption spectra with 50 μM DPA present (Figure S38a), at short delay times after the laser pulse the spectroscopic features corresponding to ^{3*}PMS are still dominant (green trace), while over time the known spectrum of ^{3*}DPA is detected.[22] Hence, the shorter lifetime of the biexponential fit is assigned to ^{3*}PMS while the longer lifetime is assigned to ^{3*}DPA. To faciliate the Stern−Volmer type analysis, the quenched triplet state lifetime was estimated from the faster component of a biexponential fit with an unquenched lifetime of 47 μs (Figure S37). The global maximum of the triplet spectrum of PMS is at 425 nm with an over three-time higher signal intensity compared to the peak at 525 nm (Figure S37 *vs* Figure S38c), but also the spectral features from the triplet of DPA are much weaker at the latter wavelength. Hence, a Stern−Volmer type analysis was mainly performed at 525 nm (Figure S37) and a bimolecular rate constant k_{TTET} of 2.4 · 10^9 M^{-1} s^{-1} is measured. Perfeclty in line with our mechanistic picture (Figure S7), with increasing concentration of DPA also a higher signal intensity at 445 nm (maximum of ^{3*}DPA) is detectable (Figure S38b). Similarly to the decay curves at 525 nm, also at 425 nm a short-lived and a long-lived decay is observed

(Figure S38c). With a similar Stern−Volmer type analysis as described above, a bimolecular rate constant of $2.0 \cdot 10^9$ M^{-1} s^{-1} is estimated for the excited state quenching of ^{3*}PMS by DPA (inset of Figure S38c).

4.4. Triplet-triplet annihilation upconversion

4.4.1. Triplet-triplet annihilation rate constants and triplet state lifetimes

Analyzing the first and second order decay pathways of the triplet state of the annihilator, the transient absorption decay curves of the annihilator triplet states are analyzed based on an analytical solution derived by Bachilo and Weisman taking both concurrent processes into account (equations S1 and S2).[23]

$$\Delta A = \frac{\Delta A_0 \cdot (1-\beta)}{\exp(k_T \cdot t) - \beta} \tag{S1}$$

$$\beta = \frac{k_{TTA} \cdot [^3A]_0}{k_{TTA} \cdot [^3A]_0 + k_T} \tag{S2}$$

The details to determine the natural lifetime τ_0 ($= k_T^{-1}$) and the triplet-triplet annihilation rate constant k_{TTA} were discussed earlier in more detail,[20,24,25] and the same methodology has been used here. For PMS (extinction coefficient at 425 nm: 25000 M^{-1} cm^{-1})[18] intersystem crossing allows a ^{3*}PMS population by direct excitation of PMS at 355 nm (Figure S39). For DPA (extinction coefficient at 415 nm: 15600 M^{-1} cm^{-1})[4] the triplet state was generated by a sensitized energy transfer from [Ru(phen)$_3$](PF$_6$)$_2$ (Figure S40). With both annihilators the determined rate constant k_{TTA} of DPA[26,27] and PMS[18] is close to the values of measurements in other solvents.
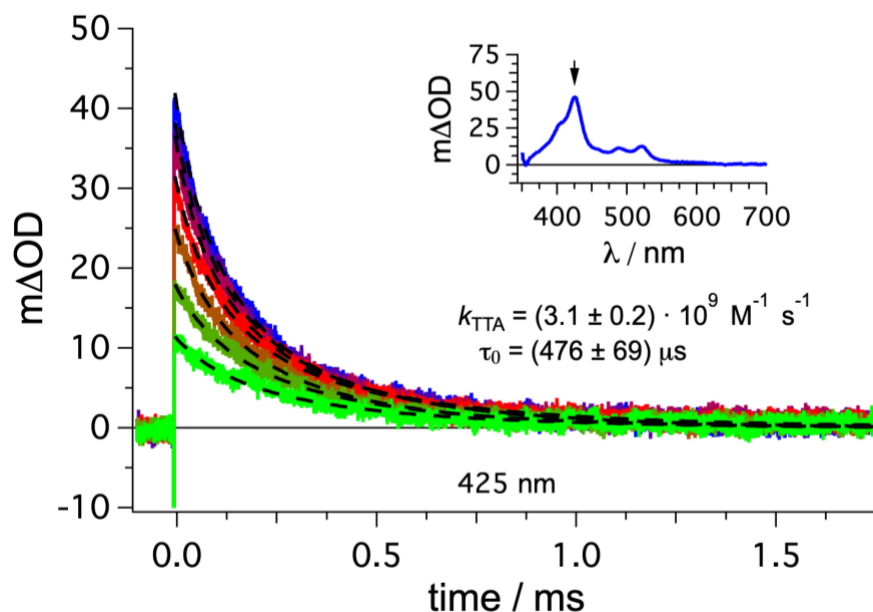
Figure S39. Power-dependent triplet state decay of PMS. PMS (150 μM) in de-aerated dimethylformamide was excited at 355 nm. Decay of transient signals of ^{3*}PMS with different excitation pulse energies were monitored at 425 nm. Fitting curves are given as dashed black traces. The inset displays the transient absoprtion spectrum of ^{3*}PMS with the detection wavelength being highlighted.
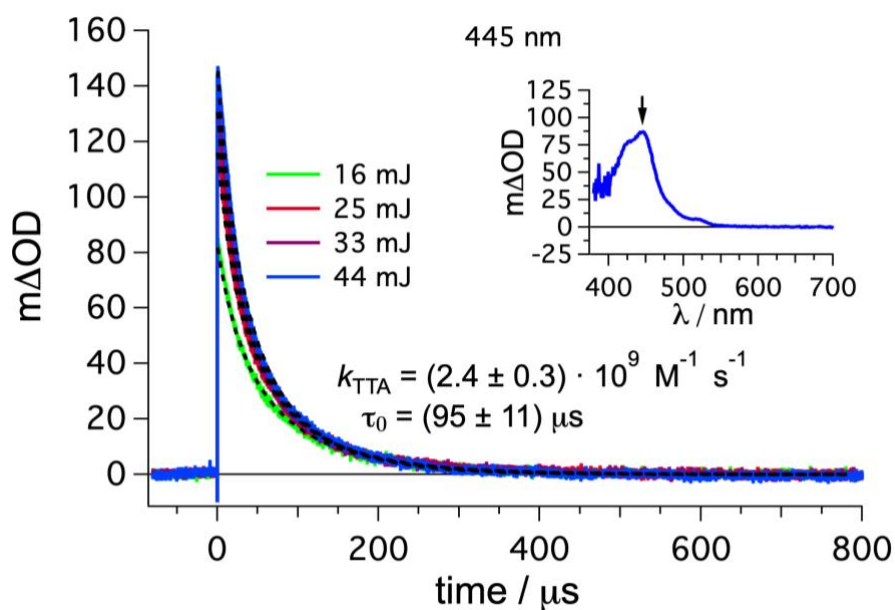
Figure S40. Power-dependent triplet state decay of DPA. [Ru(phen)$_3$]$^{2+}$ (50 μM) in de-aerated dimethylformamide was excited at 532 nm in the presence of DPA (5 mM). Decay of transient signals of ^{3*}DPA with different excitation pulse energies were monitored at 445 nm. Fitting curves are given as dashed black traces. The inset displays the transient absoprtion spectrum of ^{3*}PMS with the detection wavelength being highlighted.

4.4.2. Optimization study and first upconversion quantum yield measurements

In this section the optimization of the mediator and annihilator concentrations under steady-state irradiation conditions is presented.

Influence of DPA concentration variations in the mediated upconversion system

The relative upconversion intensity of a system with 50 μM [Ru(phen)$_3$](PF$_6$)$_2$ and 2.5 mM PMS and different concentrations of annihilator present in solution shows a fast saturation within the first 25 μM of DPA and essentially no change at higher concentrations of mediator present (Figure S41). This is in good agreement to the calcualted energy transfer efficiency of the second energy transfer step (purple trace in Figure S41). The initial emission intensity in the abesnce of DPA is caused by the weak upconversion of PMS.

Figure S41. Dependence of the upconverted emission on the DPA concentration. Steady-state emission spectra of DPA (different concentrations) upon 514 nm cw laser excitation (30 mW, 1 W cm^{-2}) of [Ru(phen)$_3$](PF$_6$)$_2$ (50 μM) in de-aerated DMF with concentrations between 0 μM to 250 μM of DPA and 2.5 mM PMS were recorded. On the left side, the individual emission spectra are presented, while on the right side the relative normalized integrated emission intensity of these traces is plotted against the annihilator concentration. The calculated energy transfer efficiency based on the energy transfer rate constant k_{TTET} from ^{3*}PMS to DPA (see Table S3) is provided as purple line (referring to the right axis).

Influence of PMS concentration in the mediated upconversion system

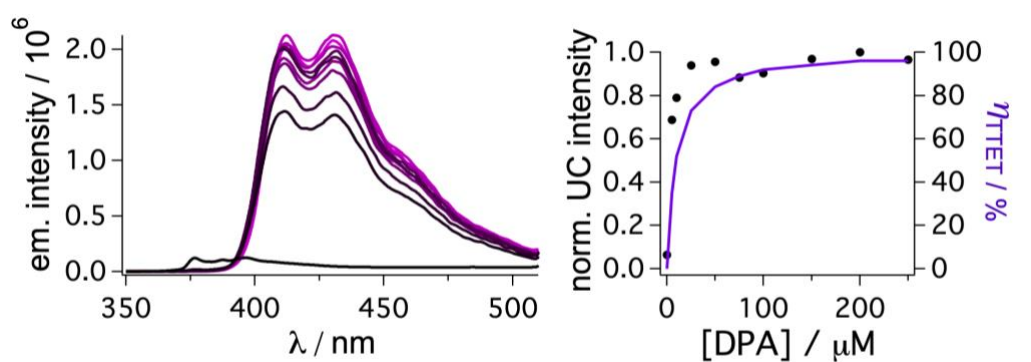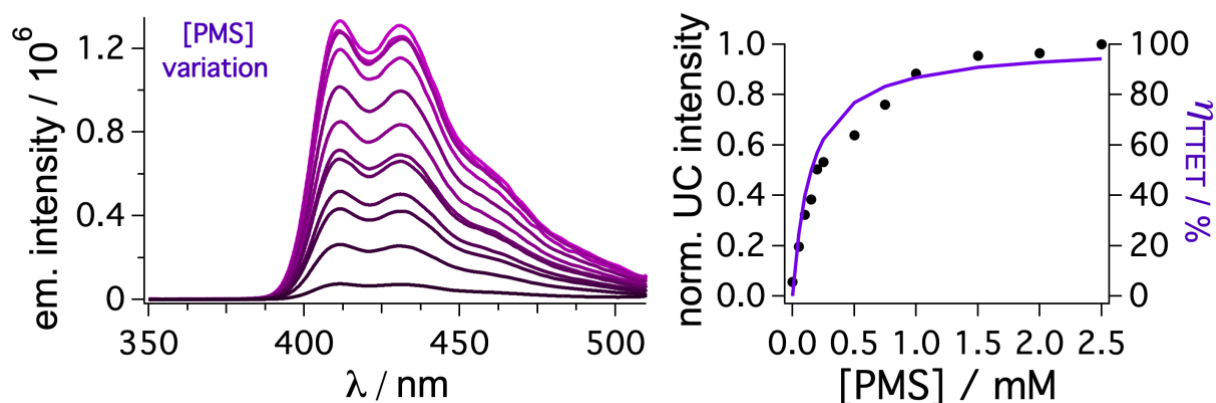**Figure S42.** Dependence of the upconverted emission on the mediator concentration. Steady-state emission spectra of DPA (100 μM) upon 514 nm cw laser excitation (30 mW, 1 W cm^{-2}) of [Ru(phen)$_3$](PF$_6$)$_2$ (50 μM) in de-aerated DMF with concentrations between 0 mM to 2.5 mM of PMS were recorded. On the left side, the individual emission spectra are presented, while on the right side the relative normalized integrated emission intensity of these traces is plotted against the mediator concentration. The calculated energy transfer efficiency based on the energy transfer rate constant k_{TTET} from [Ru(phen)$_3$]$^{2+}$ to PMS (see Table S3) is provided on the right axis (purple line).

The relative upconversion intensity of a system with 50 μM [Ru(phen)$_3$](PF$_6$)$_2$ and 100 μM DPA and different concentrations of mediator present in solution shows a straightfoward trend to more intense upconverted emission at higher concentrations of mediator present (Figure S42). The realtive integrated intensities of the upconverted light match well to the calculated energy transfer efficiencies of the first energy transfer step from ^{3*}[Ru(phen)$_3$]$^{2+}$ to PMS. Small derivations are likely caused by the equilibrium between ^{3*}[Ru(phen)$_3$]$^{2+}$ and ^{3*}PMS in the first step and general measurement inaccuracies.

Influence of sensitizer concentration in the mediated upconversion system

Optimization of the sensitizer concentration is not as straightforward as for the mediator, because several parameters are changed at once in this case. A higher sensitizer concentration results in higher absorbance at the excitation wavelength and therefore an increased number of photons absorbed. As a consequence, also the steady-state equilibrium concentrations of excited sensitizer, mediator and annihilator in solution change. In addition, the overlap between the absorption of the sensitizer and the upconverted emission of the annihilator (Figure S5) result in additional filter effects as well as unwanted FRET deactivation pathways.[28–30] Furthermore, in our special system here, where the energy difference between the sensitizer and mediator allows a back energy transfer, a higher concentration of sensitizer can introduce more deactivation *via* this pathway due to the comparable concentrations of sensitizer and annihilator. Our measurements suggest a maximum quantum yield with ~50 μM sensitizer.
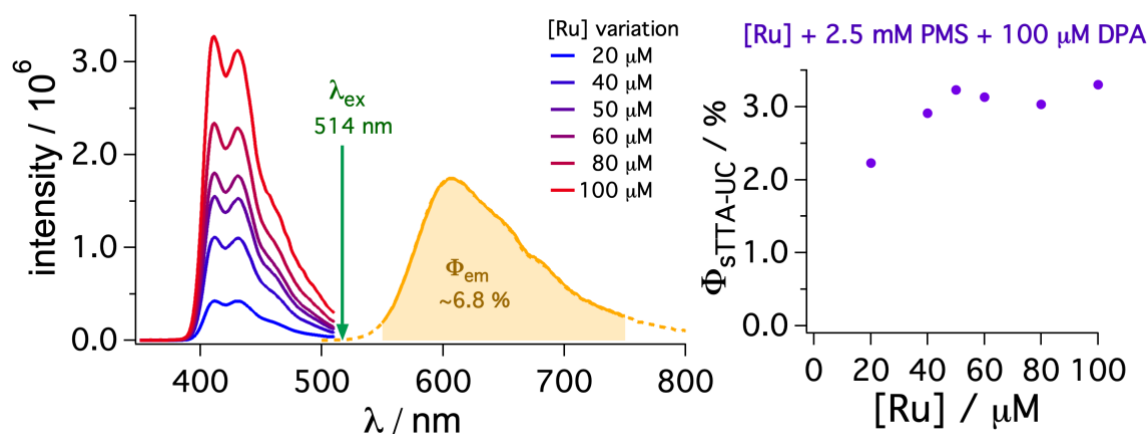
Figure S43. Dependence of the upconverted emission on the sensitizer concentration. Steady-state emission spectra of DPA (100 μM) were recorded upon 514 nm cw laser excitation (30 mW, 1 W cm^{-2}) of [Ru(phen)$_3$](PF$_6$)$_2$ (50 μM) in de-aerated DMF in the presence of PMS (2.5 mM) as mediator. All upconversion quantum yields were measured against the emission of [Ru(phen)$_3$](PF$_6$)$_2$ in de-aerated DMF with an identical concentration as in the upconversion sample. Here only the reference emission with 50 μM [Ru(phen)$_3$](PF$_6$)$_2$ is shown and the other reference spectra are omitted for clarity.

Initial test on the power dependence in the mediated upconversion system
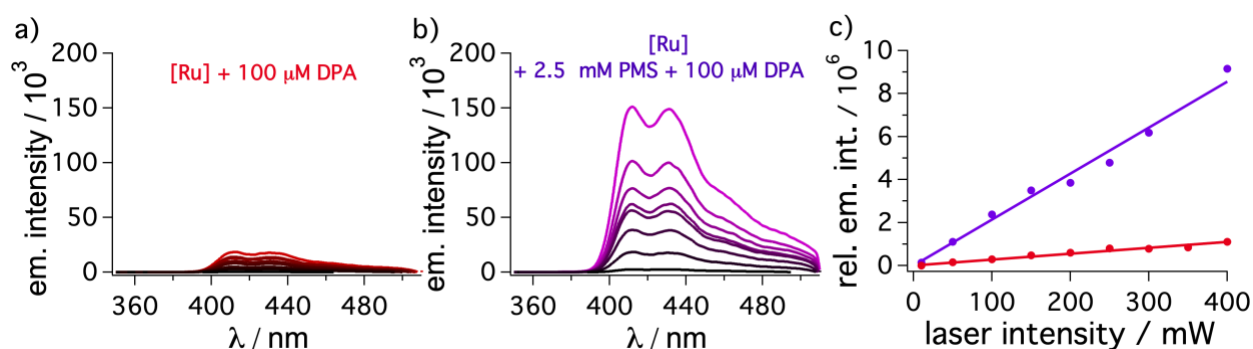
Figure S44. Power dependence of the upconverted emission in the presence and absence of mediator. Steady-state emission spectra of DPA (100 μM) upon 514 nm cw laser excitation of [Ru(phen)$_3$](PF$_6$)$_2$ (50 μM) in de-aerated DMF in the absence (a) and presence (b) of PMS (2.5 mM) as mediator. c) Relative integrated emission intensities in dependence to the laser power of the excitation light source.

Initial measurements of the power dependence were performed with laser intensities between 50 and 400 mW (corresponding to power densities of 1.7 W cm^{-2} to 13.3 W cm^{-2}). A linear correlation between the upconverted emission and the laser intensity were observed (Figure S44). This is clear evidence that the threshold intensity is below these power densities explored here and the strong annihilation limit with a linear dependence is reached in these measurements. This nicely complements the threshold intensity measurements presented in the Figure 5 of the main manuscript with significantly lower power densities utilized to visualize the quadratic

dependence. The improvement with a factor of ~8 comparing the data in the presence and absence of mediator is in line with the upconversion quantum yields determined at 1 W cm^{-2}.

4.4.3. Power dependence and upconversion quantum yield estimation

Upconversion quantum yield estimation

The upconversion quantum yield ($\phi_{sTAA-UC}$) was measured as relative value in comparison to the unquenched prompt phosphorescence of $[Ru(phen)_3]^{2+}$ in de-aerated DMF (ϕ_{Ref} = 6.8%) and the same absorption at the excitation wavelength. The relative quantum yield is calculated with equation S3. The absorbance at the excitation wavelength (A), the integrated emission[2] (I) and the refractive index of the solvent (η) are required for the upconversion system (denoted with subscript UC) and the reference system (denoted with subscript Ref) under identical conditions.

$$\phi_{sTTA-UC} = \phi_{Ref} \cdot \frac{A_{Ref}}{A_{UC}} \cdot \frac{I_{UC}}{I_{Ref}} \cdot \frac{\eta_{UC}^2}{\eta_{Ref}^2} \qquad \text{(S3)}$$

The determined upconversion quantum yields using a laser as light source are presented in the main manuscript and reference measurements are presented hereafter. In addition, the datasets obtained with an LED as light source are presented here.

Expected improvement factor based on the energy transfer rate constants

The energy transfer efficiency η_{TTET} can be calculated based on the quenched (τ) and unquenched lifetimes (τ_0) of the respective states (equation S4).

$$\eta = 1 - \frac{\tau}{\tau_0} \qquad \text{(S4)}$$

To determine the quenched lifetime, a rearranged Stern–Volmer equation is utilized together with the known concentrations of quencher Q and the determined rate constants k_{TTET} (Table 1 of the main manuscript).

$$\tau = \left(\frac{1}{\tau_0} + k_Q \cdot [Q]\right)^{-1} \quad \tau = \left(\frac{1}{\tau_0} + k_{TTET} \cdot [Q]\right)^{-1} \qquad \text{(S5)}$$

Taking into consideration the lifetime of $^{3*}[Ru(phen)_3]^{2+}$ (728 ns) and $^{3*}PMS$ (476 µs) together with the different energy transfer rate constants (Table S3), the overall energy transfer efficiency of the product of the individual steps from $^{3*}[Ru(phen)_3]^{2+}$ to PMS (η_{TTET1} = 93.4%) and from $^{3*}PMS$ to DPA (η_{TTET2} = 92.3%) is 87.1% and this about ~6.9 times higher than the efficiency for the direct energy transfer from $^{3*}[Ru(phen)_3]^{2+}$ to DPA (η_{TTET} = 12.7%) under the conditions utilized in our upconversion system. The calculated improvement factor is reasonably close to the measured enhancement of the upconversion quantum yield in the presence and absence of mediator (~6.4). For comparison, the direct energy transfer with 5 mM of DPA is almost identical with respect to energy transfer efficiency (η_{TTET} = 87.9%) and therefore a reasonable comparison with respect to the filter effect is possible.

Quadratic power dependence and upconversion quantum yield estimation with cw laser as light source

The threshold intensity measurements are shown in Figure 5 of the main manuscript. The laser intensity was modulated by the introduction of different neutral density filters (Thorlabs) between the cw laser and the cuvette (Figure S3). The excitation power was subsequently corrected for the transmittance of the filter at the excitation wavelength. To maximize the emission intensity at the detector the laser beam was adjusted to hit the sample closer to the glass wall near the detector.

In order to obtain a complete picture of the upconversion processes and the different systems investigated herein, in addition to the measurements in Figure 5 of main manuscript the upconversion quantum yield of PMS as annihilator (Figure S45) was investigated. PMS turned out to be a poorly upconverting annihilator, likely due to a combination of several factors such as the comparably low fluorescence quantum yield (Table S1), ionic repulsion between the charged annihilators,[25] the excited state equilibrium between ^{3*}PMS and ^{3*}[Ru(phen)$_3$]$^{2+}$ (section 4.2.5) and the special geometry of the PMS triplet pair potentially reducing the productivity of TTA with this pyrene derivative (section 4.2.5).
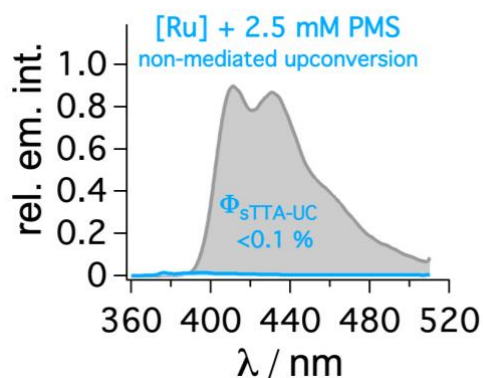
Figure S45. Upconverted emission sensitized by [Ru(phen)$_3$]$^{2+}$ ([Ru], 50 μM) in de-aerated DMF at 20 °C. Excitation occurred with a 514 nm cw laser. Upconversion quantum yield $\Phi_{sTTA-UC}$ with PMS (2.5 mM) in the absence of DPA determined relative to the [Ru(phen)$_3$]$^{2+}$ emission (not shown, Φ_{em} = ~6.8%). The quantum yield was measured in triplicate with a laser intensity of 30 mW (1 W cm^{-2}).

Quadratic power dependence and upconversion quantum yield estimation with an LED as light source

Similar to the measurements with a cw laser as light source, the power dependence measurements were also performed with a 525 nm LED equipped with a 495 nm longpass filter (Newport). Again, the modulation of the excitation intensity was performed by the introduction of neutral density filter (Thorlabs) in the light pathway. For the integration of the emission traces to determine relative quantum yields, the measured emission spectra were corrected for contributions caused by the LED and consequently the dotted lines in Figure S46b were analyzed.

Figure S46. Power dependence and upconversion quantum yields with an LED as light source. a) Steady state emission spectra of DPA (100 μM) upon excitation of [Ru(phen)$_3$](PF$_6$)$_2$ (50 μM) in the presence of PMS (2.5 mM) in de-aerated dimethylformamide were measured at different irradiation intensities (Kessil 525 nm, 40 W). The light intens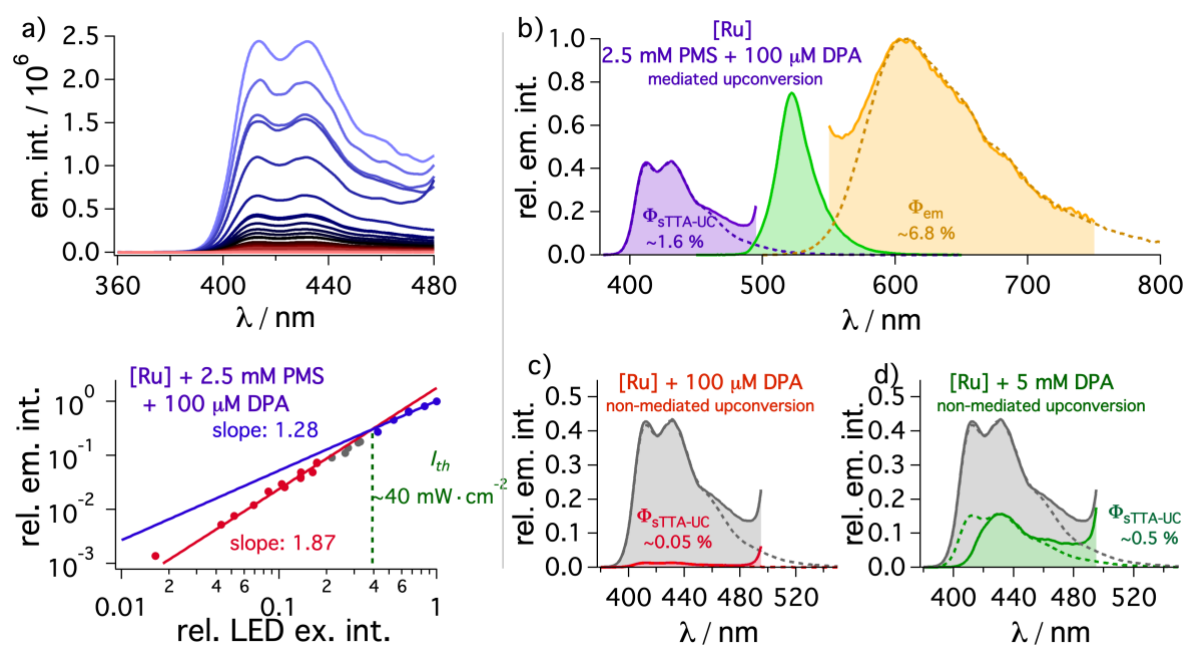ity was modulated by neutral density filters between the LED and the cuvette. A double-logarithmic graph of integrated emission intensities against the relative LED excitation light source intensity is presented below the emission spectra. (b-d) Upconversion quantum yields Φ$_{sTTA-UC}$ with DPA (100 μM) in the (b) presence and (c) absence of PMS (2.5 mM) determined relative to the [Ru(phen)$_3$]$^{2+}$ emission (ocher trace, Φ$_{em}$ = ~6.8%). d) Additional measurement with high concentrations of DPA (5 mM) in the absence of mediator. All quantum yields were measured in duplicate at the highest LED intensity (40 W, ~100 mW cm^{-2}).

The non-parallel spherical light output of the LED complicates an exact analysis of the measurements. In addition, the power density in the cuvette is highly dependent on the exact distance between the sample and the LED. Hence, especially the power dependence measurements with an LED as light source have several uncertainties and the absolute values need to be handled with care.

Nevertheless, several interesting insights into our system can be obtained from these measurements. First of all, our data indicate that the LED can provide a power density above the threshold intensity of our system (Figure S46a). However, at a distance that allows the installation and exchange of different neutral density filter the power density is only ~100 mW cm^{-2} according to the general intensity map provided by the manufacturer. As a consequence, the strong annihilation limit is not yet reached with this setup. Secondly, as indicated by the LED intensity that is only in the transition region between the quadratic and linear regime of the annihilation process, the full upconversion quantum yield is not reached. As a consequence, the measured upconversion quantum yield is smaller than the value determined with a cw laser (Figure S46b). Thirdly, the reference measurements without mediator in solution (Figure S46c) or with high concentrations of DPA (Figure S46d) are significantly smaller compared to the datasets with a cw laser light source. This indicates,

that for an irradiation of the full reaction flask the filter effects are even more pronounced compared to the optimized measurements with the cw laser.

4.4.4. Stability measurements

The stability of the upconversion system over time was measured with a 514 nm cw laser (30 mW, 1 W cm^{-2}). It is worth mentioning that the emission setup does not provide an active cooling and thermal degradation by heating of the sample cannot be excluded.

Stability under continuous laser irradiation
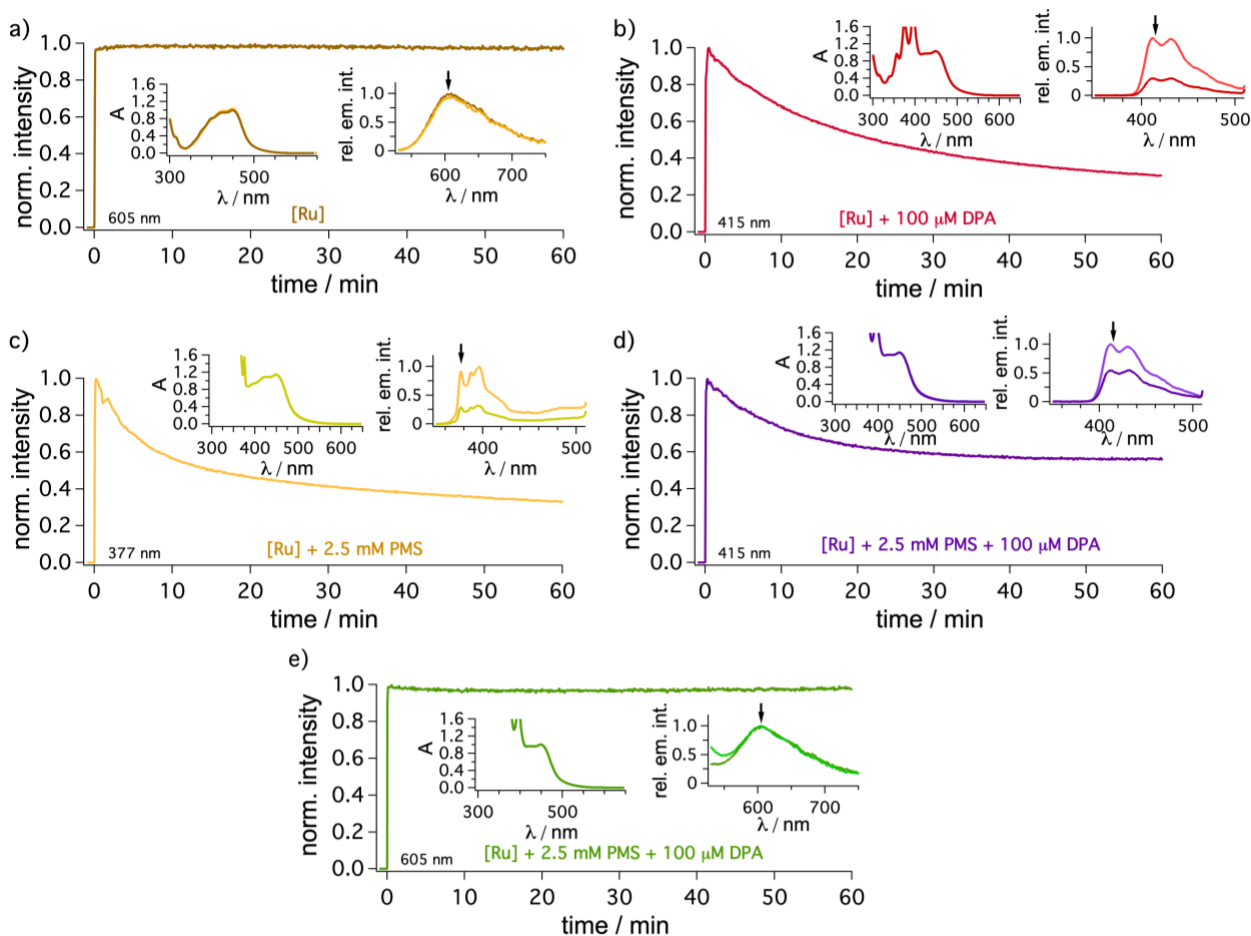
Figure S47. Photostability under cw laser irradiation. Solutions of [Ru(phen)$_3$](PF$_6$)$_2$ (50 μM) in DMF were combined with DPA (b), PMS (c), as well as both DPA and PMS (d, e) and the emission decay was detected at the emission maximum over time. In all cases with these components present, the initial concentrations of DPA (100 μM), PMS (2.5 mM) were identical to the measurments discussed in the main manuscript and all measurements were performed in de-aerated solutions. Before (light traces) and after 60 minutes of irradiation (dark traces), UV-vis and emission spectra were recorded and presented here as insets. In panel (a) and (e) the ruthenium-based emission at 600 nm was detected.

The stability measurements indicate a limited stability of all upconversion samples investigated here (Figure S47b-e). In contrast, the sensitizer emission is stable under these conditions in the absence of any quencher

(Figure S47a) as well as in the presence of PMS and DPA (Figure S47e). While a decomposition of the mediator in the full system would be expected to result in an increasing emission from the sensitizer over time, a constant emission over time implies, that the initial energy transfer to PMS is unaffected and a decomposition of DPA is likely responsible for the decreasing upconversion signals over time. Nevertheless, the mediated system with PMS (Figure S47d) gave best stability results among the three tested upconversion systems.

4.4.5. Filter effect

To receive qualitative insights into the inner filter effect caused by the ground state absorption of the annihilator, the emission spectra were recorded with different concentrations of DPA in aerated solution (Figure S48). At low concentrations (up to 100 µM), the relative intensity increases owing to the increasing absorption at the excitation wavelength. Between 100 µM and 1 mM DPA, the relative intensity is slightly diminished and the high-energy vibrational band becomes smaller with increasing concentrations. Above 1 mM DPA the high-energy vibrational band is completely vanished and in addition the overall emission intensity decreases.
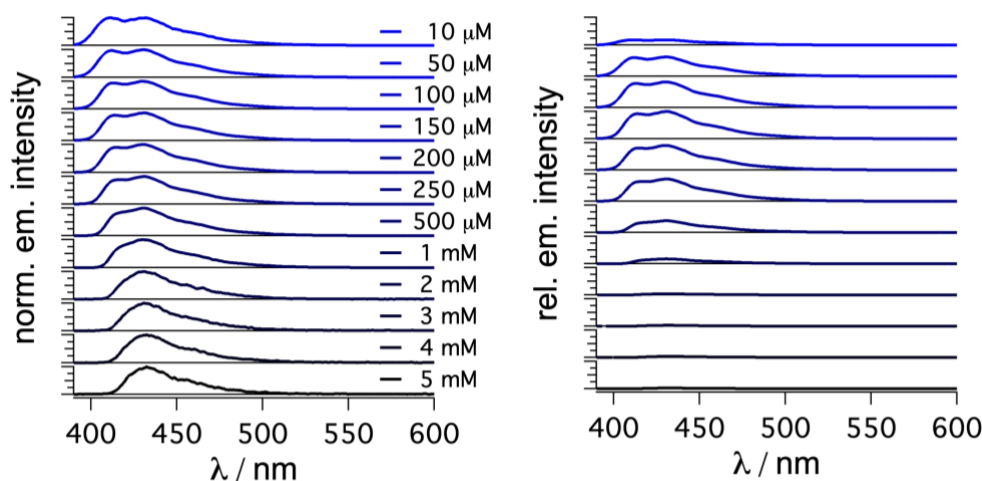
Figure S48. Detectable emission at different concentrations of DPA. Different concentrations of DPA in aerated DMF were excited at 380 nm and the fluorescence was detected under standardized excitation and detection conditions. The concentration of each sample is indicated in the figure. All measurements were performed with the same instrumental settings of the steady-state emission spectrometer. The datasets are presented with a relative intensity scale (right) and a normalized intensity scale (left).

4.5. Analyzing the sensitizer-mediator interactions

$$[Ru(phen)_3]^{2+} \;+\; PMS^{-} \rightleftharpoons [Ru(phen)_3](PMS)^{+}$$

$$K_A = \frac{[[Ru](PMS)]}{[Ru] \cdot [PMS]} \tag{S6}$$
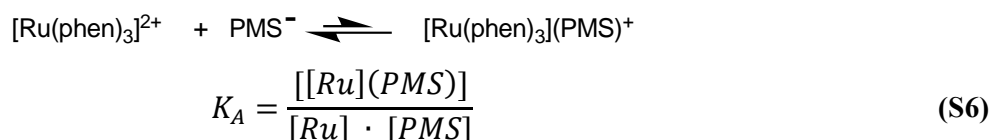
There are different methods to determine the 1:1 association constant between two species in solution according to equation S6.

Here we focus on the use of ^{1}H NMR titration in DMF and DMSO as solvents (section 4.5.1),[31–33] while the analysis by time-resolved spectroscopy seems less accurate and is only briefly discussed (section 4.5.2).[34]

4.5.1. Association constant determined by ^{1}H NMR spectroscopy

^{1}H NMR titration in DMF

The determined association constant K_A in DMF-d_7 using a Benesi–Hildebrand analysis is ~30 ($\pm$ 2) M^{-1}. The corresponding ^{1}H NMR spectra are provided in Figure 4 of the main manuscript.

^{1}H NMR titration in DMSO

The determined association constant K_A in DMSO-d_6 using a Benesi–Hildebrand analysis is ~35 ($\pm$ 4) M^{-1}. The corresponding ^{1}H NMR spectra are provided in Figure S49. The association constant is very close to the value determined in DMF-d_6.
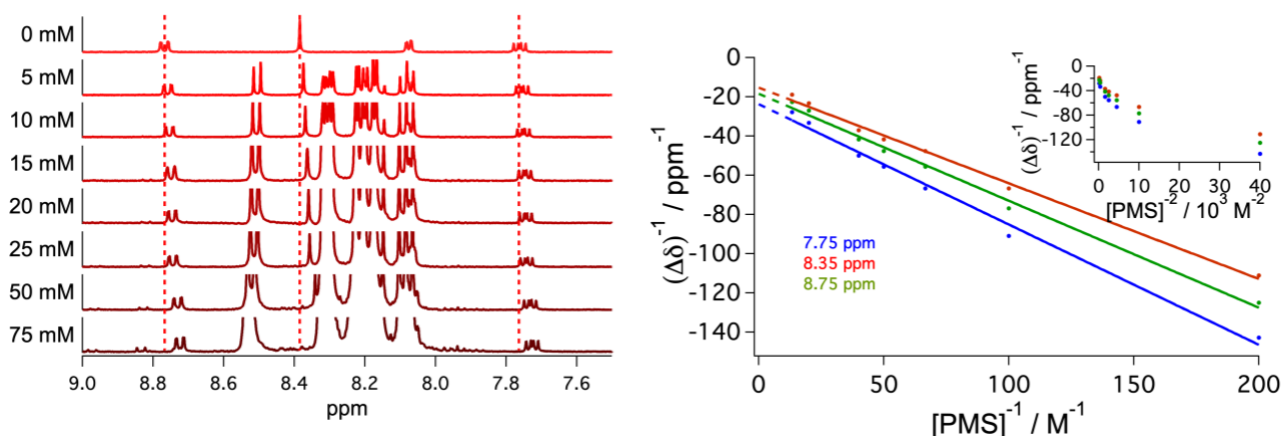
Figure S49. ^{1}H NMR titration of different concentrations of PMS to a solution of [Ru(phen)$_3$]$^{2+}$ (500 µM) in DMSO-d_6 and the corresponding Benesi–Hildebrand plot (bottom) following the peaks of [Ru(phen)$_3$]$^{2+}$ at different chemical shifts δ. The determined association constant K_A is ~35 ($\pm$ 4) M^{-1}. The inset presents the same raw datasets with a linearization for a possible 1:2 association. A comparison between the 1:1 and 1:2 linearization clearly indicates a better fit for the 1:1 stoichiometry.[35]

4.5.2. Association constant estimated by kinetic emission measurements

In principle, also time-resolved emission data should have a concentration-dependent initial emission amplitude as an association between energy donor and acceptor results in static quenching.[36,37] In our case, estimated K_A values for the association between $[Ru(phen)_3]^{2+}$ and PMS vary between ~33 ($\pm$ 8) M^{-1} based on the maximum of the kinetic traces and ~75 ($\pm$ 12) M^{-1} based on the intensities determined from the kinetic fit curves at the time of laser pulse (t = 0 ns). Due to the comparably small extinction coefficient of $[Ru(phen)_3]^{2+}$ at the excitation wavelength of 532 nm, the absorbance of the complex is comparably low (A = ~0.04) at the utilized concentrations (50 μM). With small changes of the absorbance, possibly caused by the formation of supramolecular complexes between $[Ru(phen)_3]^{2+}$ and PMS, the determined values for K_A might not be perfectly accurate. From a more quantitative view, the initial amplitude of the emission of $[Ru(phen)_3]^{2+}$ in the presence of 0 and 2 mM of PMS, the initial intensity lower by about 10%. This is in line with a minor contribution from static quenching and is close to the value that was calculated based on the association constant determined by ^{1}H NMR spectroscopy (see main manuscript for details).
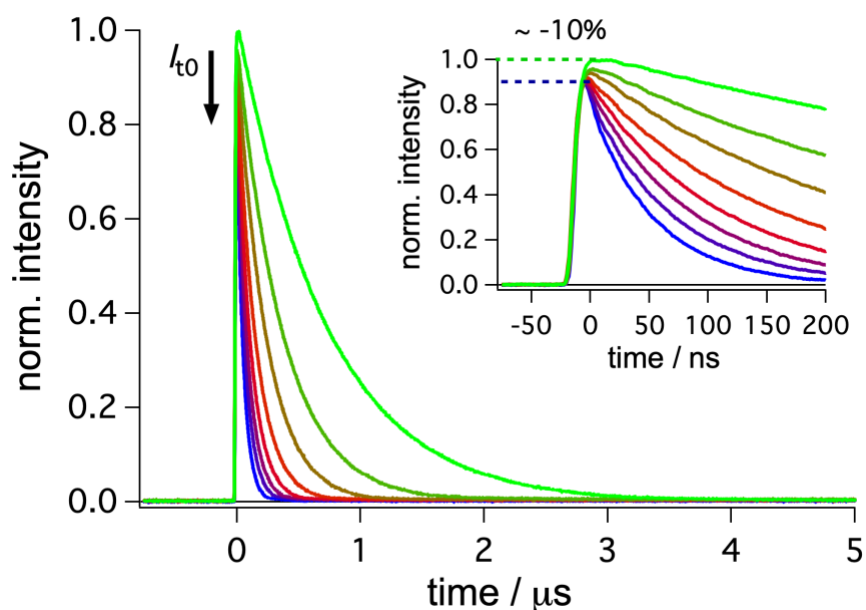
Figure S50. Emission lifetime quenching of $^{3*}[Ru(phen)_3]^{2+}$ by PMS. $[Ru(phen)_3]^{2+}$ (50 μM) in de-aerated dimethylformamide was excited at 532 nm (standardized laser intensity) and the emission decay was monitored at 600 nm in the absence (green) and in the presence of different concentrations of PMS (0.10, 0.25, 0.5, 0.75, 1.0, 1.5, 2.0 mM). The pre- and post-pulse region is shown on enlarged scale as the inset.

4.6. Applications for photocatalysis

4.6.1. Concepts for upconversion in the presence of oxygen

The difference concepts for light-driven catalysis using sTTA-UC in the presence of oxygen are summarized in Figure S51.

Figure S51. Schematic representation of different concepts using sensitized triplet-triplet annihilation upconversion with molecular oxygen present in solution for possible application on photo(redox) catalysis. The systems rely on interception of singlet oxygen by scanvengers,[38] enzymatic deox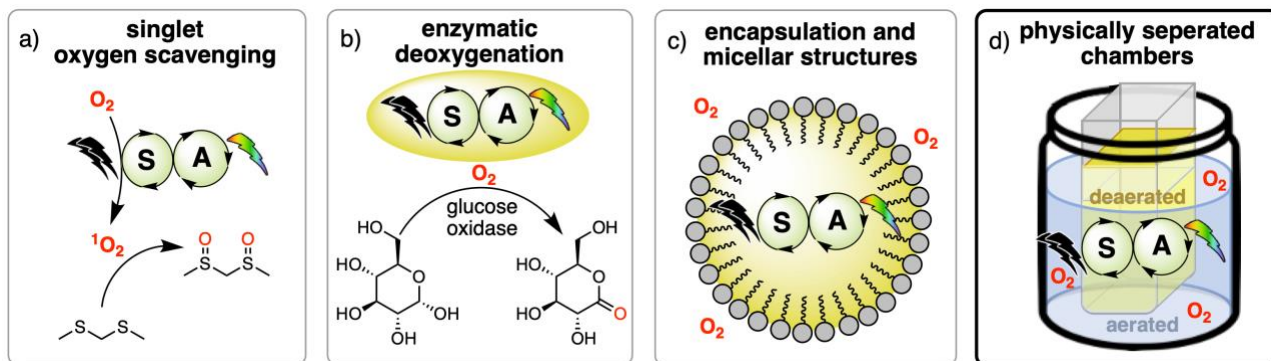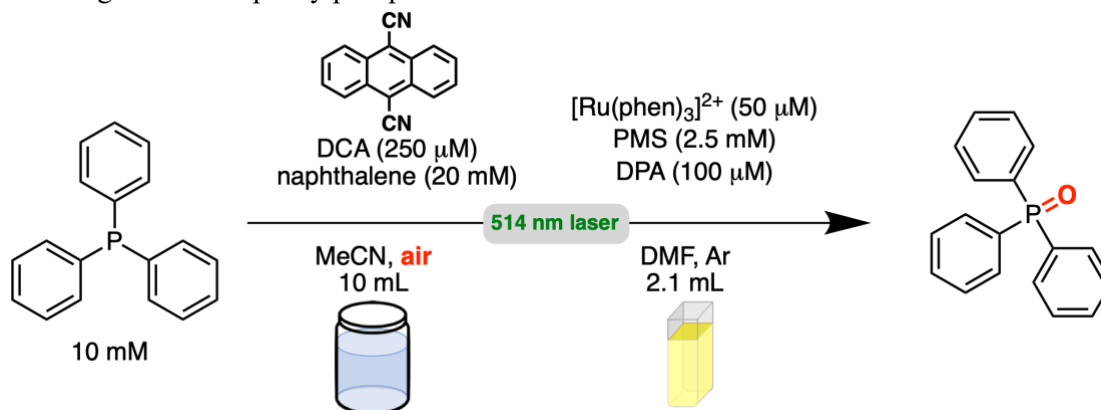ygenation,[39] encapsulation of the upconversion system and micellar structures,[40–48] and with two separated chambers.

4.6.2. Triphenylphosphine oxidation

Table S6. Light-driven triphenylphosphine oxidation with DCA.[a]

[Ru(phen)₃](PF₆)₂	PMS	DPA	additional change	conversion / %[b]
50 μM	2.5 mM	100 μM	-	90
50 μM	-	100 μM	-	26
50 μM	-	5 mM	-	74
50 μM	2.5 mM	-	-	26
50 μM	-	-	-	15
50 μM	-	100 μM	no DCA	6
50 μM	2.5 mM	100 μM	no laser excitation	8

a) The general procedure is provided in section 3.1.2. All samples were irradiated for 20 minutes with a cw laser (514 nm, 800 mW) and the conversion of triphenylphosphine was measured after removal of the solvent. The irradiation setup is provided in Figure S3. b) Conversion determined by ^{1}H NMR spectroscopy.

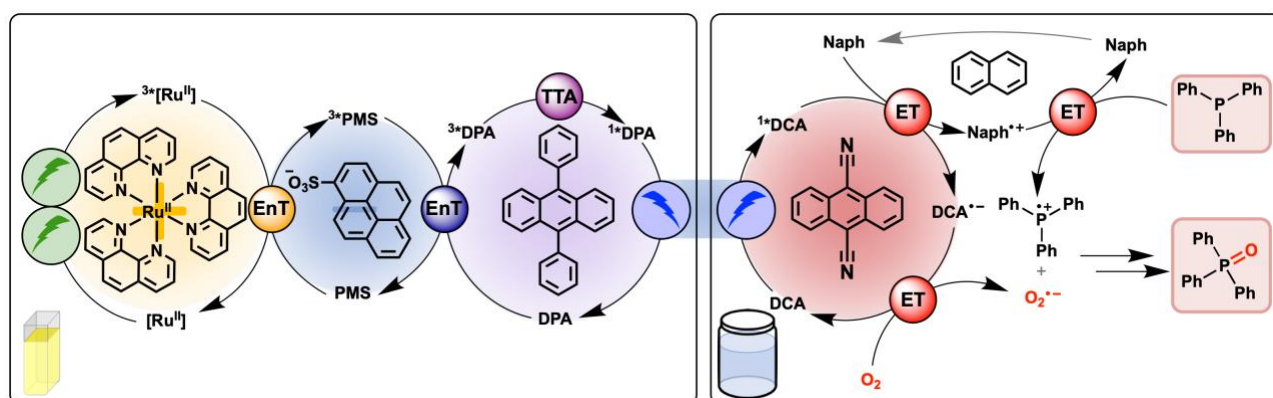**Proposed mechanism for the triphenylphosphine oxidation**

Figure S52. Proposed mechanism for the phosphine oxidation by DCA in the presence of naphthalene as redox mediator (right) using sensitized mediated TTA-UC (left) to generate blue light emission.

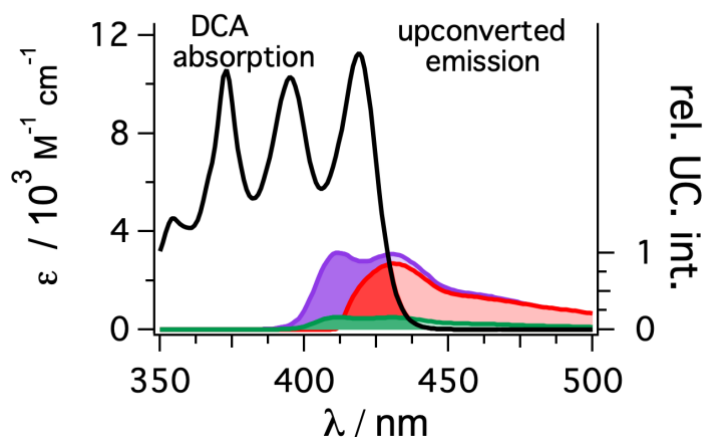**Spectral overlap between 9,10-dicyanoanthracene and the upconversion systems**

Figure S53. Spectral overlap between the photosensitizer (DCA, black trace) and the normalized upconverted emission of DPA with [Ru(phen)$_3$](PF$_6$)$_2$ (50 μM) in de-aerated DMF as sensitizer in the absence (green) or presence of 2.5 mM PMS (purple) or with 5 mM of DPA (red). The emission spectra are identical to the datasets in Figure 3 of the main manuscript, but the additional absorbance from an irradiation in the middle of the cuvette (~4-5 mm pathway for the upconverted light within the cuvette) and the emission spectra detection with a beam closer to the detector of the instrument (~1-2 mm pathway for the upconverted light within the cuvette).

A comparison between the absorbance of DCA and the upconverted emission of DPA under different conditions (Figure S53) clearly illustrate that the largest spectral overlap is possible with the complete sensitizer-mediator-annihilator combination (purple spectrum), followed by the sample with high concentrations of DPA (red trace) and then a significantly smaller overlap with the non-mediated upconversion system (green trace). This is in perfect agreement with measured differences in the photocatalytic performance (Table S6).

4.6.3. Anthracene endoperoxide formation

Light-driven catalysis

Table S7. Light-driven endoperoxide formation with MeOTX. [a]

[Ru(phen)₃](PF₆)₂	PMS	DPA	additional change	conversion / % [b]
50 µM	2.5 mM	100 µM	-	71
50 µM	-	100 µM	-	21
50 µM	-	5 mM	-	28
50 µM	-	-	-	14
50 µM	2.5 mM	100 µM	no MeOTX	37
50 µM	2.5 mM	100 µM	no laser excitation	~0
-	-	-	- [c]	11

a) The general procedure is provided in section 3.1.3. All samples were irradiated for 150 minutes with a cw laser (514 nm, 800 mW) and the conversion of 9,10-dimethylanthracene was determined by the change in absorbance of DMAn in the UV-vis spectra measured in 2 mm cuvettes. The irradiation setup is provided in Figure S3. b) Conversion determined by the spectral change at 358 nm in the UV-vis spectra measured in 2 mm cuvettes. The datasets in this table are uncorrected values. c) Cuvette with DMF in the absence of any catalyst.
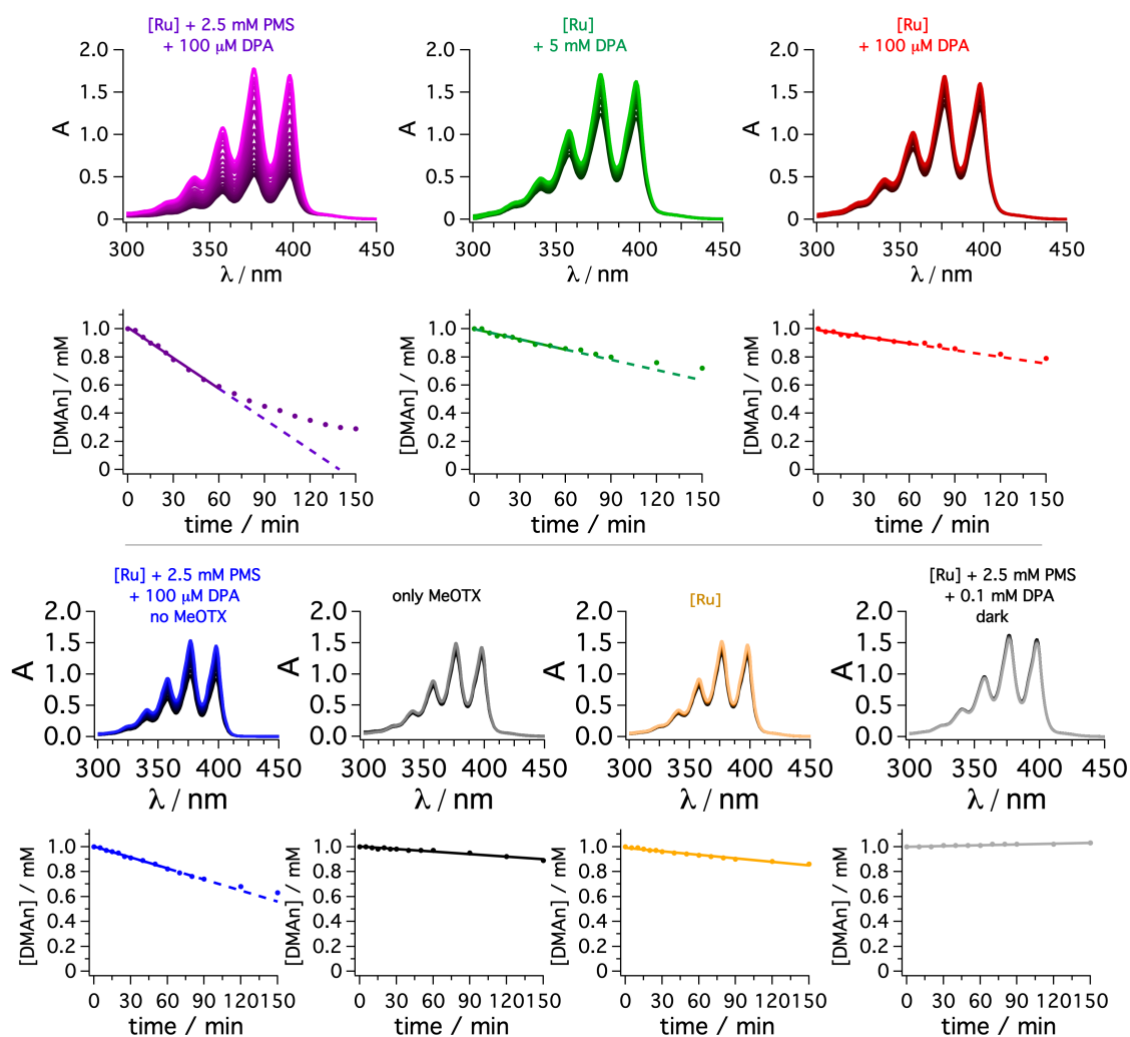
Figure S54. UV-vis absorption spectra and DMAn concentration changes over time under different conditions. The different upconversion solutions in the cuvette are indicated as insets (reaction conditions are indicated in Table S7) and the spectra were measured in 2 mm cuvettes.

Table S8. Analysis of the DMAn endoperoxide formation with MeOTX. [a]

$[Ru(phen)_3](PF_6)_2$	PMS	DPA	additional changes	$-\Delta c\,\Delta t^{-1}$ / $\mu M\ min^{-1}$ [b]	corrected $-\Delta c\,\Delta t^{-1}$ / $\mu M\ min^{-1}$ [c]	*relative ratio* [d]
50 µM	2.5 mM	100 µM	-	7.27	6.73	6.4
50 µM	-	100 µM	-	1.59	1.05	1.0
50 µM	-	5 mM	-	2.43	1.89	1.8
50 µM	-	-	-	1.16	0.62	0.6
50 µM	2.5 mM	100 µM	no laser excitation	-	-	-
-	-	-	- [e]	0.54	0	-

a) The exact reaction conditions are provided in Table S7. b) The concentration of DMAn was estimated based on the absorbance at 358 nm and concerted to the concentration. The change over time was subsequently determined from the temporal evolution over the first 60 minutes of irradiation (see Figure S54). c) The change over time ($-\Delta c\,\Delta t^{-1}$) is corrected for the observed background reactivity in the absence of any catalyst of the upconversion system ($-\Delta c\,\Delta t^{-1} = 0.54\ \mu M\ min^{-1}$). d) Relative ratio between the corrected slopes for the sensitizer-annihilator system in the absence of mediator (second entry of this table, $-\Delta c\,\Delta t^{-1} = 1.05\ \mu M\ min^{-1}$) and the corrected change over time of the respective measurement in the corresponding entry. e) Cuvette with DMF in the absence of any catalyst.

Table S9. Overlap integral for MeOTX catalyzed DMAn reaction with $^1O_2$. [a]

[Ru(phen)$_3$](PF$_6$)$_2$	PMS	DPA	*relative ratio overlap integral* [b]	*relative ratio conversion* [c]
50 µM	2.5 mM	100 µM	4.9	6.4
50 µM	-	100 µM	1.0	1.0
50 µM	-	5 mM	2.5	1.8

a) Overlap integral between MeOTX absorption and upconverted emission, calculated MeOTX and the fluorescence of the donors normalized to the upconversion emission of the full sensitizer-mediator-annihilator system (main manuscript Figure 8).[36] b) Relative ratio between the overlap integrals of the respective entry and the non-mediated upconversion system (overlap color-coded in Figure 8 of the main manuscript). c) Relative ratio between the corrected concentration changes over time for the non-mediated upconversion system and the corrected change over time with the indicated reaction conditions (see Figure **S55**).

The two-chamber approach to combine de-aerated sensitized triplet-triplet annihilation upconversion with aerated endoperoxide formation introduces the possibility to directly measure the absorbance of DMAn in solution. The contribution from the photocatalyst MeOTX at 358 nm is negligible under the utilized conditions (< 5%, see Figure S56) and consequently the concentration of the DMAn reactant after different irradiation times can be calculated at this wavelength. Surprisingly, reference measurements in the complete absence of any catalyst in the cuvette also resulted in a slow substrate degradation over time and a comparison to a measurement in the absence of cw laser irradiation clearly points towards a light-induced process here (Figure S54 and Table S8). The measured slopes for the change in DMAn concentration over time (Figure S54) were therefore corrected for the background reactivity by a subtraction of the respective slopes for the determined slope in the absence of any catalyst ($-\Delta c\, \Delta t^{-1} = 0.54$ µM min^{-1}) and the results are summarized in Table S8. These corrected slopes are subsequently compared to the spectral overlap between the upconverted emission and the absorbance of the photocatalyst. The factor for the enhancement with our mediator system in comparison to other conditions (calculated as relative ratio of the rates or overlap integrals) were in good agreement (Table S9) and this clearly illustrates the beneficial properties of our system.

MeOTX in aerated and de-aerated acetonitrile

The decay of ^{3*}MeOTX detected at 625 nm by transient absorption spectroscopy in the presence and absence of oxygen with averaged lifetimes of ~19 µs for ^{3*}MeOTX under argon and 110 ns in aerated solution clearly shows efficient oxygen quenching (>99%). With an oxygen solubility in air-saturated acetonitrile (2.42 mM)[49], a rate constant for oxygen quenching is about ~$4 \cdot 10^9$ M^{-1} s^{-1}. Hence, this organic sensitizer is in principle suitable as photocatalyst for endoperoxide formation *via* the generation of $^1O_2$.
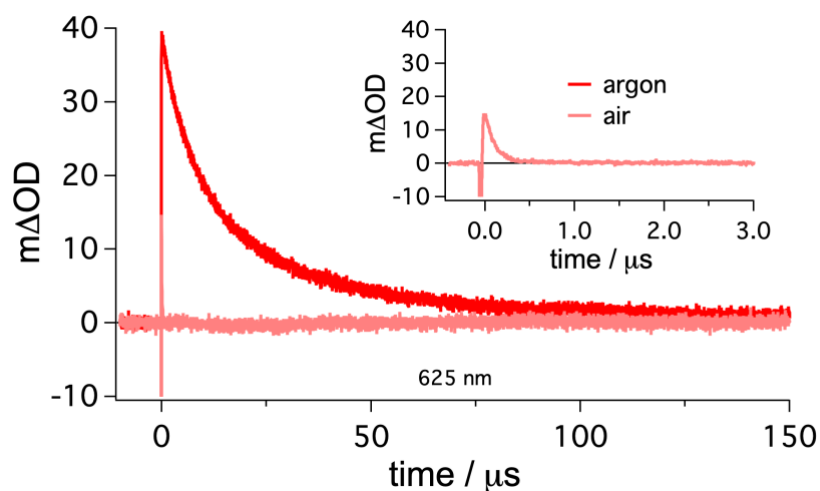
Figure S55. Decay of ^{3*}MeOTX in aerated and de-aerated solution. MeOTX (200 μM) in aerated (pale red) and de-aerated (dark red) acetonitrile was excited at 355 nm and the triplet state decay was monitored at 625 nm. The inset displays a measurement of the aerated solution on a shorter time scale of 3 μs. A transeint absorption spectum of MeOTX is also presented in Figure S6.

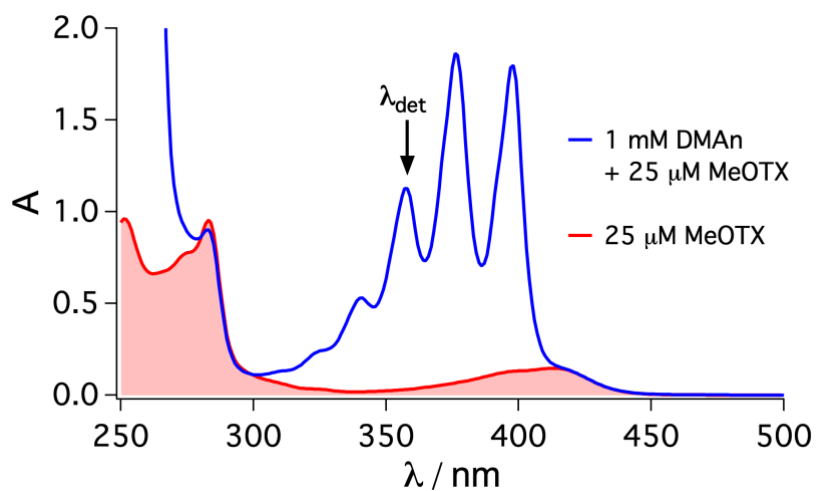**Spectral overlap between MeOTX photocatalyst and DMAn substrate**

Figure S56. UV-vis absorption spectra of MeOTX (25 μM) in acetonitrile in the absence (red) and presence (blue) of DMAn (1 mM). The spectra were recorded with 2 mm cuvettes and the wavelength for the concentration determination of DMAn is highlighted.

5.   Additional NMR spectra
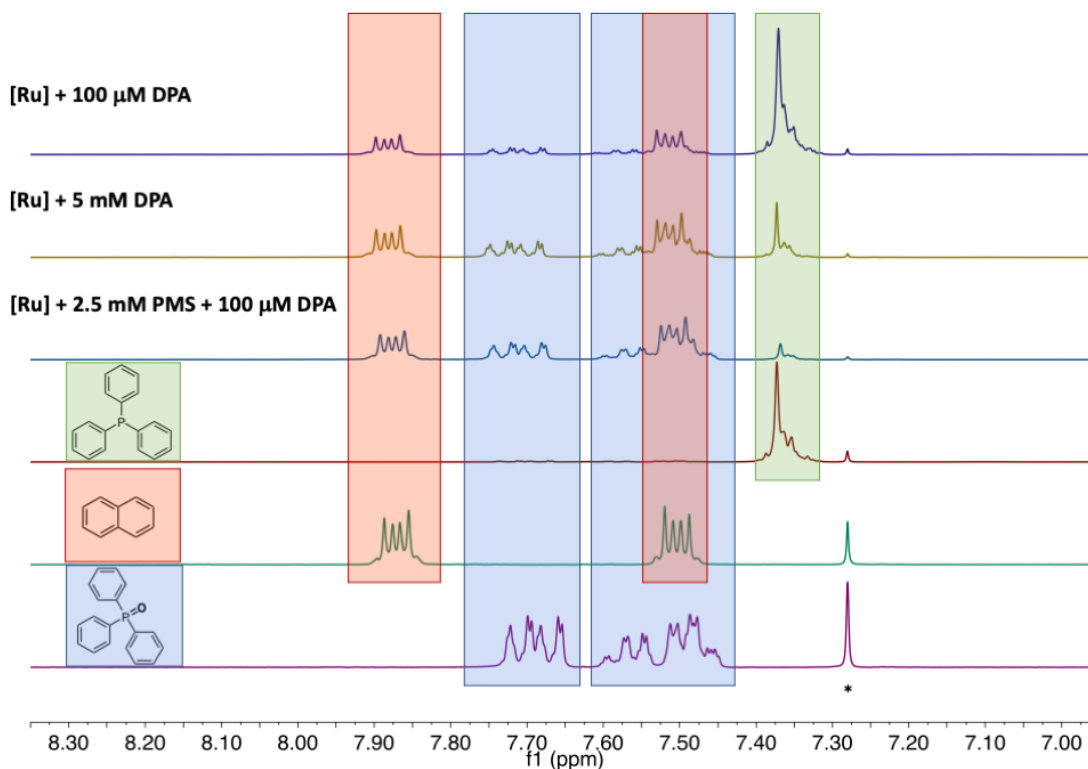
Figure S57. ^{1}H NMR spectra of light-driven photocatalytic triphenylphosphine oxygenation *via* sTTA-UC with different upconversion systems (first three panels) and reference ^{1}H NMR spectra of triphenylphosphine, naphthalene and triphenylphosphine oxide (last three panels) in CDCl$_3$. The peak corresponding to non-deuterated solvent (CHCl$_3$) is marked with an asterisk. Detailed reaction conditions are provided in section 3.1.2. *Synthetic procedure for triphenylphosphine oxide synthesis:* triphenylphosphine (19.7 mg, 75 μmol) and DCA (2 mol%) were dissolved in acetonitrile (5 mL) and irradiated (40 W 427 nm Kessil LED) for 1 hour under constant oxygen-purging. After removal of the solvent the product was isolated by preparative thin layer chromatography.

6. References

1   N. R. Patel, C. B. Kelly, M. Jouffroy and G. A. Molander, *Org. Lett.*, 2016, **18**, 764–767.

2   J. Mooney and P. Kambhampati, *J. Phys. Chem. Lett.*, 2013, **4**, 3316–3318.

3   J. Castellanos-Soriano, D. Álvarez-Gutiérrez, M. C. Jiménez and R. Pérez-Ruiz, *Photochem. Photobiol. Sci.*, 2022, **21**, 1175–1184.

4   M. Montalti, A. Credi, L. Prodi and M. T. Gandolfi, *Handbook of Photochemistry*, CRC Press: Taylor & Francis Group, Boca Raton, FL, USA, 3rd edn., 2006.

5   K. Suzuki, A. Kobayashi, S. Kaneko, K. Takehira, T. Yoshihara, H. Ishida, Y. Shiina, S. Oishi and S. Tobita, *Phys. Chem. Chem. Phys.*, 2009, **11**, 9850–9860.

6   G. A. Crosby and J. N. Demas, *J. Phys. Chem.*, 1971, **75**, 991–1024.

7   L. Wang, P. Cui, B. Liu, S. Kilina and W. Sun, *Dalton Trans.*, 2018, **47**, 13776–13780.

8   Z. Ji, S. D. Huang and A. R. Guadalupe, *Inorg. Chim. Acta*, 2000, **305**, 127–134.

9   H. Iranmanesh, K. S. A. Arachchige, M. Bhadbhade, W. A. Donald, J. Y. Liew, K. T. C. Liu, E. T. Luis, E. G. Moore, J. R. Price, H. Yan, J. Yang and J. E. Beves, *Inorg. Chem.*, 2016, **55**, 12737–12751.

10   A. A. Vlcek, E. S. Dodsworth, W. J. Pietro and A. B. P. Lever, *Inorg. Chem.*, 1995, **34**, 1906–1913.

11   T. H. Tran-Thi, C. Prayer, P. Millié, P. Uznanski and J. T. Hynes, *J. Phys. Chem. A*, 2002, **106**, 2244–2255.

12   M. Yang, S. Sheykhi, Y. Zhang, C. Milsmann and F. N. Castellano, *Chem. Sci.*, 2021, **12**, 9069–9077.

13   H. Moon, Y. W. Jun, D. Kim, H. G. Ryu, T. Wang, K. H. Kim, Y. Huh, J. Jung and K. H. Ahn, *Chem. Asian J.*, 2016, **11**, 2518–2523.

14   L. D. Elliott, S. Kayal, M. W. George and K. Booker-Milburn, *J. Am. Chem. Soc.*, 2020, **142**, 14947–14956.

15   F. Glaser and O. S. Wenger, *JACS Au*, 2022, **2**, 1488–1503.

16   S. J. Horsewill, G. Hierlmeier, Z. Farasat, J. P. Barham and D. J. Scott, *ACS Catal.*, 2023, 9392–9403.

17   C. E. McCusker and F. N. Castellano, *Chem. Commun.*, 2013, **49**, 3537–3539.

18   C. Bohne, E. B. Abuin and J. C. Scaiano, *J. Am. Chem. Soc.*, 1990, **112**, 4226–4231.

19   C. Ye, V. Gray, J. Mårtensson and K. Börjesson, *J. Am. Chem. Soc.*, 2019, **141**, 9578–9584.

20   F. Glaser, C. Kerzig and O. S. Wenger, *Chem. Sci.*, 2021, **12**, 9922–9933.

21   M. S. Coles, G. Quach, J. E. Beves and E. G. Moore, *Angew. Chem. Int. Ed.*, 2020, **59**, 9522–9526.

22   C. Wang, F. Reichenauer, W. R. Kitzmann, C. Kerzig, K. Heinze and U. Resch-Genger, *Angew. Chem. Int. Ed.*, 2022, **61**, e202202238.

23   S. M. Bachilo and R. B. Weisman, *J. Phys. Chem. A*, 2000, **104**, 7713–7714.

24   F. Glaser and O. S. Wenger, *Chem. Sci.*, 2023, **14**, 149–161.

25   B. Pfund, D. M. Steffen, M. R. Schreier, M.-S. Bertrams, C. Ye, K. Börjesson, O. S. Wenger and C. Kerzig, *J. Am. Chem. Soc.*, 2020, **142**, 10468–10476.

26   A. Olesund, V. Gray, J. Mårtensson and B. Albinsson, *J. Am. Chem. Soc.*, 2021, **143**, 5745–5754.

27   V. Gray, A. Dreos, P. Erhart, B. Albinsson, K. Moth-Poulsen and M. Abrahamsson, *Phys. Chem. Chem. Phys.*, 2017, **19**, 10931–10939.

28   T. J. B. Zähringer, J. A. Moghtader, M.-S. Bertrams, B. Roy, M. Uji, N. Yanai and C. Kerzig, *Angew. Chem. Int. Ed.*, 2023, **62**, e202215340.

29   Y. Zhou, F. N. Castellano, T. W. Schmidt and K. Hanson, *ACS Energy Lett.*, 2020, **5**, 2322–2326.

30   D. V. Kozlov and F. N. Castellano, *Chem. Commun.*, 2004, **1**, 2860–2861.

31   P. Thordarson, *Chem. Soc. Rev.*, 2011, **40**, 1305–1323.

32   L. Fielding, *Tetrahedron*, 2000, **56**, 6151–6170.

33   H. A. Benesi and J. H. Hildebrand, *J. Am. Chem. Soc.*, 1949, **71**, 2703–2707.

34   D. Genovese, M. Cingolani, E. Rampazzo, L. Prodi and N. Zaccheroni, *Chem. Soc. Rev.*, 2021, **50**, 8414–8427.

35   J. W. Park, in *Cyclodextrin Materials Photochemistry, Photophysics and Photobiology*, ed. Abderrazzak Douhal, Elsevier, Amsterdam, 2006, pp. 1–26.

36   J. R. Lakowicz, *Principles of Fluorescence Spectroscopy*, Springer US, Boston, MA, 2006.

37   L. Troian-Gautier, W. B. Swords and G. J. Meyer, *Acc. Chem. Res.*, 2019, **52**, 170–179.

38   D. Dzebo, K. Moth-Poulsen and B. Albinsson, *Photochem. Photobiol. Sci.*, 2017, **16**, 1327–1334.

39   L. Huang, T. Le, K. Huang and G. Han, *Nat. Commun.*, 2021, **12**, 1898.

40   M. Häring, R. Pérez-Ruiz, A. Jacobi von Wangelin and D. D. Díaz, *Chem. Commun.*, 2015, **51**, 16848–16851.

41   F. Marsico, A. Turshatov, R. Peköz, Y. Avlasevich, M. Wagner, K. Weber, D. Donadio, K. Landfester, S. Baluschev and F. R. Wurm, *J. Am. Chem. Soc.*, 2014, **136**, 11057–11064.

42   S. Baluschev, K. Katta, Y. Avlasevich and K. Landfester, *Mater. Horizons*, 2016, **3**, 478–486.

43   P. Bharmoria, S. Hisamitsu, H. Nagatomi, T. Ogawa, M. A. Morikawa, N. Yanai and N. Kimizuka, *J. Am. Chem. Soc.*, 2018, **140**, 10848–10855.

44   H. Kouno, Y. Sasaki, N. Yanai and N. Kimizuka, *Chem. Eur. J.*, 2019, **25**, 6124–6130.

45   H. Lee, M. S. Lee, M. Uji, N. Harada, J. M. Park, J. Lee, S. E. Seo, C. S. Park, J. Kim, S. J. Park, S. H. Bhang, N. Yanai, N. Kimizuka, O. S. Kwon and J. H. Kim, *ACS Appl. Mater. Interfaces*, 2022, **14**, 4132–4143.

46   R. Jeyaseelan, M. Utikal, C. G. Daniliuc and L. Næsborg, *Chem. Sci.*, 2023, **14**, 11040–11044.

47   S. N. Sanders, T. H. Schloemer, M. K. Gangishetty, D. Anderson, M. Seitz, A. O. Gallegos, R. C. Stokes and D. N. Congreve, *Nature*, 2022, **604**, 474–478.

48   O. S. Kwon, J. H. Kim, J. K. Cho and J. H. Kim, *ACS Appl. Mater. Interfaces*, 2015, **7**, 318–325.

49   C. Franco and J. Olmsted, *Talanta*, 1990, **37**, 905–909.